

AD-A119 961

NAVAL RESEARCH LAB WASHINGTON DC

F/G 20/4

VORTICITY GENERATION BY ASYMMETRIC ENERGY DEPOSITION IN A GASEO--ETC(U)

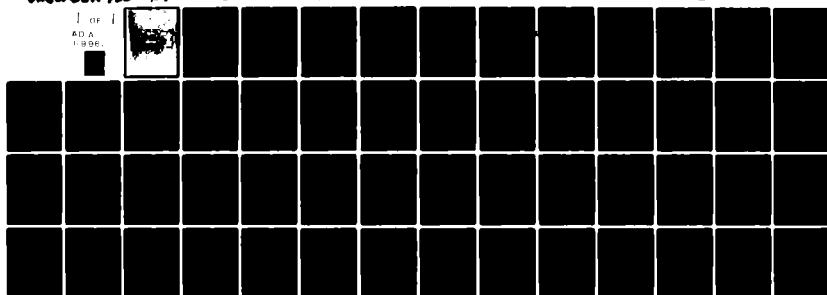
SEP 82 J P BORIS, J M PICONE

NL-1P-4854

NL

UNCLASSIFIED

1 OF 1
AD A
1 806



END
DATE
FILMED
DTIC

AD A17 9001

SECURITY CLASSIFICATION OF THIS PAGE (When Data Entered)

REPORT DOCUMENTATION PAGE		READ INSTRUCTIONS BEFORE COMPLETING FORM
1. REPORT NUMBER NRL Memorandum Report 4854	2. GOVT ACCESSION NO. AD A11996	3. RECIPIENT'S CATALOG NUMBER 1
4. TITLE (and Subtitle) VORTICITY GENERATION BY ASYMMETRIC ENERGY DEPOSITION IN A GASEOUS MEDIUM	5. TYPE OF REPORT & PERIOD COVERED Interim report on a continuing project	
7. AUTHOR(s) J. P. Boris and J. M. Picone	6. PERFORMING ORG. REPORT NUMBER	
9. PERFORMING ORGANIZATION NAME AND ADDRESS Naval Research Laboratory Washington, D.C. 20375	8. CONTRACT OR GRANT NUMBER(s)	
11. CONTROLLING OFFICE NAME AND ADDRESS DARPA Arlington, VA 22209	10. PROGRAM ELEMENT PROJECT, TASK AREA & WORK UNIT NUMBERS 44-0580-0-2 61101E/DARPA 3718	
14. MONITORING AGENCY NAME & ADDRESS (if different from Controlling Office) Naval Surface Weapons Center White Oak Silver Spring, MD 20910	12. REPORT DATE September 16, 1982	
	13. NUMBER OF PAGES 55	
	15. SECURITY CLASS. (of this report) UNCLASSIFIED	
	15a. DECLASSIFICATION/DOWNGRADING SCHEDULE	
16. DISTRIBUTION STATEMENT (of this Report) Approved for public release; distribution unlimited		
17. DISTRIBUTION STATEMENT (of the abstract entered in Block 20, if different from Report)		
18. SUPPLEMENTARY NOTES		
19. KEY WORDS (Continue on reverse side if necessary and identify by block number) Charged particle beam Gas channel cooling Hydrodynamics Holeboring Gas channel formation		
20. ABSTRACT (Continue on reverse side if necessary and identify by block number) This paper develops in detail the theory of vorticity generation by asymmetries which are present when a cylindrical pulse of energy is deposited in a gaseous medium. We identify three classes of asymmetry which may occur separately or in combination, depending on the experiment being analyzed. We also introduce a convenient representation of the flow field in terms of one or more vortex filament pairs having identical strengths. The equations which give the vortex filament strength for the various asymmetry classes differ only in the value of a form factor, which contains information regarding geometric effects and hydrodynamic interactions. The form factor, however. (Continued)		

DD FORM 1 JAN 73 1473

EDITION OF 1 NOV 65 IS OBSOLETE
S/N 0102-014-6601

SECURITY CLASSIFICATION OF THIS PAGE (When Data Entered)

20. ABSTRACT (Continued)

depends only weakly on the profile of the density distribution of the medium prior to energy deposition. Finally we verify and calibrate the analytic results by providing data from accurate two-dimensional simulations of several cases. The analytic and numerical calculations agree closely for all examples considered.

CONTENTS

I.	INTRODUCTION	1
II.	MECHANISMS FOR CONVECTIVE COOLING	2
III.	MIXING TIME SCALE	3
	A. Vortex Filament Representation	3
	B. Derivation of Mixing Time Scale	4
	C. Estimates of τ_{mix} from Dimensional Analysis	7
IV.	APPROXIMATE VORTICITY INTEGRALS	8
	A. Off Center Beam Propagation	10
	B. Two-Dimensional Distortion (Elliptical Channel)	16
	C. Three-Dimensional Distortions	19
	D. Nonuniform Deposition of Energy	21
V.	DETAILED NUMERICAL SIMULATIONS	22
	A. Off Center Pulse Propagation	23
	B. Two-Dimensional Distortions	27
VI.	CONCLUSIONS	28
	ACKNOWLEDGMENTS	29
	REFERENCES	29



Accession For	
NTIS GRA&I	<input checked="" type="checkbox"/>
DTIC TAB	<input type="checkbox"/>
Unannounced	<input type="checkbox"/>
Distribution	
Distribution/	
Availability Codes	
Avail and/or	
Dist Special	
A	

VORTICITY GENERATION BY ASYMMETRIC ENERGY DEPOSITION IN A GASEOUS MEDIUM

I. INTRODUCTION

Recent experiments by Greig et al.¹⁻⁵ have studied hot channels produced by lasers and electric discharges in ambient air. Following expansion to pressure equilibrium, the hot channels cool with a rate which is several orders of magnitude faster than that attributable to classical thermal conduction. Since any reasonable estimate of background gas velocities falls far short of explaining the cooling rate, we require a mechanism to convert curl-free fluid expansion, which does not mix, into persistent vorticity, which can. The importance of determining the mechanisms and scaling laws governing the dynamics and cooling of such hot channels derives from the application of discharge physics to other areas, such as beam physics and the study of nitrogen fixation in the atmosphere by lightning.⁵ In the latter case, the cooling rate of the hot channel gas is critical to predicting the global production of nitrogen oxides.

In Section II of this paper we propose a mechanism for the generation of persistent flows which mix cold, ambient gas into the hot gaseous channels produced by one or more pulses of energy. The mechanism relies on deviations from cylindrical symmetry in energy deposition by a given pulse, and we identify three classes of asymmetry which appear to be physically significant. Section II also introduces a convenient representation of the vorticity distribution in terms of one or more vortex filament pairs. We use this representation in Section III to derive a formula for the mixing time scale τ_{mix} , which characterizes the rate at which cool ambient air is entrained into the hot channel. To estimate τ_{mix} , we use dimensional analysis to derive an approximate formula for the expansion induced vorticity. Our estimate shows that the proposed mechanism causes mixing of cool background gas with the heated channel interior on time scales which are orders of magnitude shorter than those characterizing molecular thermal conduction. Section IV provides a detailed theoretical analysis of the three classes of asymmetry. The resulting formulae for the vorticity strength are considerably more accurate than that of Section III. Section V presents the results of detailed two-dimensional simulations of several sample cases. These computations validate the qualitative features predicted by the analytic model and permit us to calibrate the analytic formulae accompanying the model. We have used our results to analyze experimental data on the cooling of electric discharge channels.⁵ Our comparisons have indicated good agreement between predicted and observed mixing times.

II. MECHANISMS FOR CONVECTIVE COOLING

The symmetric expansion of a cylindrical channel, produced by a pulse of energy causes no convective mixing per se, but asymmetries in energy deposition which are inherent in the pulse structure or which occur relative to the local density distribution generate long-lived vortex filaments. The sheared flow attending the motion and interaction of these filaments mixes cold background gas into the heated channel at a rate which depends on the strength of the induced vorticity and thus ultimately on the fluid-dynamic asymmetries. We can identify three generic types of asymmetries: (1) two-dimensional asymmetries from pulse displacement off the axis of an existing hot channel, (2) two-dimensional distortions of the pulse envelope from a circular cross section, and (3) three-dimensional distortions (e.g., curvature) of the envelope, such as characterize a lightning or spark channel.

As the channel of the most recent pulse expands to pressure equilibrium, any deviations from cylindrical symmetry will lead to asymmetries between the gradients of the pressure and density distributions. The equation which describes the resulting vorticity distribution and evolution is

$$\frac{d\xi}{dt} + \xi \nabla \cdot \underline{v} = \xi \cdot \nabla \underline{v} + (\nabla \rho \times \nabla P) / \rho^2 \quad (1)$$

where

$$\xi = \nabla \times \underline{v} \quad (2)$$

is the vorticity, \underline{v} is the fluid velocity, ρ is the density, and P is the pressure. All of the variables are functions of the position \underline{r} and the time t . Following expansion of the channel to achieve pressure equilibrium, significant residual vorticity exists. This vorticity is responsible for mixing ambient gas with the hot channel gas. Here we should note that other mechanisms for generating residual vorticity in the heated channel may exist. As the channel expands to pressure equilibrium, for example, the Rayleigh-Taylor instability could grow significantly. The experimental data do not support this possibility, however.⁵ Another possibility is the rapid movement of the discharge current axis which could result from magnetic forces present when the current is nonnegligible. This could, in turn, displace the surrounding air sufficiently to produce some long-term mixing motion. We do not attempt to estimate the magnitude of such phenomena in this paper.

Figures 1-3 depict the classes of asymmetry schematically and will form the basis for our notation and calculations, as discussed in subsequent sections. While all three types will often occur simultaneously, we will treat them separately to isolate their respective characteristics. We have defined the z -axis to be collinear with the channel axis (i.e., outward from the page to the reader) for cases 1 and 2. For our analysis of three-dimensional distortions, we have chosen a section of the channel with

moderate sinusoidal curvature relative to the length. The z -axis is collinear with the center of the mass of the section. The displacement X_0 represents the degree of asymmetry which is present in a given situation.

Figure 1 shows how we model the first asymmetry class, which is relevant to sequences of approximately collinear pulses and to pulses with interior "hot spots." Our model assumes a preformed, hot, low density channel in which the next pulse is propagating off center. In Fig. 2 we present the cross section of the pulse as elliptical where the ellipticity is defined by the parameter X_0 . Residual vorticity will be present whenever X_0 is nonzero. Such a distortion of a pulse may occur in several ways: (1) the envelope of the pulse undergoes smooth spatial oscillations; (2) the pulse is deposited in a region with an azimuthally nonuniform local density distribution; or (3) the source of the pulse produces an azimuthally nonuniform (though smooth) distribution of energy. Figure 3 shows a simple model of the last asymmetry class, which includes all pulses with a curved axis. Such curved discharges occur both in laboratory discharges and in lightning.⁵ We have found that all three types of asymmetry will produce a sizable nonzero value for ξ_z which will cause mixing in the (r, θ) plane. In the case of three-dimensional distortions, ξ_θ will also be nonnegligible; this results in mixing in the (r, z) plane.

III. MIXING TIME SCALE

A. Vortex Filament Representation

We may represent the residual vorticity distribution in terms of one or more vortex filament pairs of strength $\pm \bar{\kappa}_{i\alpha}$, where the index i labels the asymmetry class and α denotes z or θ . The quantity $\bar{\kappa}_{i\alpha}$ is the integral of the vorticity over the domain containing a given filament. For example, in the case of a pulse which is noncollinear with a preformed hot channel (asymmetry type 1) we have the (x, y) flow pattern depicted in Fig. 4. These flows are equivalent to those of a single vortex filament pair having strengths of $\pm \bar{\kappa}_{1z}$ and respective locations $(\bar{x}, \pm \bar{y})$. The strength $\bar{\kappa}_{1z}$ is given by the integral of the vorticity over the upper half plane, i.e.,

$$\bar{\kappa}_{1z}(\tau) = \int_0^\infty dy \int_{-\infty}^\infty dx \xi_z(x, y, \tau) \quad (3)$$

and the coordinates are

$$\bar{x}(\tau) = \frac{1}{\bar{\kappa}_{1z}(\tau)} \int_0^\infty dy \int_{-\infty}^\infty dx x \xi_z(x, y, \tau) \quad (4)$$

and

$$\bar{y}(\tau) = \frac{1}{\bar{\kappa}_{1z}(\tau)} \int_0^\infty dy \int_{-\infty}^\infty dx y \xi_z(x, y, \tau). \quad (5)$$

The quantity τ is the time interval over which vorticity generation is completed and is thus approximately the time required for the hot channel gas to expand to pressure equilibrium. Defining $t = 0$ to be the time at which the discharge is initiated, we may integrate Eq. (1) over the interval $(0, \tau)$ to obtain the vorticity distribution $\xi_z(x, y, \tau)$.

Figure 2 shows that the elliptical channel will have two associated vortex filament pairs. Here the domain of integration in Eqs. (3)-(5) will be the quarter plane and we will use cylindrical coordinates. For the curved channel section in Fig. 3, we will again use cylindrical coordinates. The integral for $\bar{\kappa}_{1z}$ will cover the upper half plane as in Eqs. (3)-(5); however, unlike class one, $\bar{\kappa}_{1z}$ will vary along the channel axis. To obtain $\bar{\kappa}_{3\theta}$ we will integrate over half a wavelength in our simple model of a sinusoidally curved channel. Because $\bar{\kappa}_{3\theta}$ will, in general, vary with θ , we may then perform an azimuthal integral ($\theta \in [0, \pi]$) to obtain a total longitudinal mixing strength.

B. Derivation of Mixing Time Scale

In order to derive an equation for the time scale of the mixing of cool ambient gas with the hot channel gas, we must first review the experimental observations.¹⁻⁵ Soon after the deposition of energy ($\approx 300 - 600 \text{ J/m}$) by an electric discharge or laser pulse, the hot channel expands, producing a shock wave. Within $100 \mu\text{s}$, the shock has decoupled from the channel, which has reached pressure equilibrium and ceased to expand. At that point, the channel boundaries are smooth. However after another $100 \mu\text{s}$, the edges of the channel have become distorted, and the channel has started to expand and cool through entrainment of the surrounding air. By $\approx 1 \text{ ms}$, small scale (turbulent) structure is evident and the channel has grown considerably. We attribute the initial disruption of the channel and the entrainment of ambient air to the convective motion generated by the mechanism of Eq. (1). To determine the mixing time scale, therefore, we will treat this large scale structure separately from the smaller scale motion observed as the channel cools. An understanding of the development of the latter flow structure would, of course, be necessary for an accurate description of the dynamics of the fluid inside the channel.

For simplicity we assume that the asymmetry induced flow field may be represented approximately as two compact vortex filaments of strength $\pm \bar{\kappa}$ at $\pm \bar{y}$, as in Fig. 4; thus we treat each vortex filament pair separately. This is in fact the situation for ξ_z in the case of off center beam propagation. The azimuthal velocity induced by each filament decays as $1/r$ away from the vortex center. The velocity of

the fluid along the symmetry plane is the sum of flows induced by each vortex separately. Figure 4 is a schematic of the situation with a sketch of the variation of the fluid flow velocity along the x -axis. This velocity is given by

$$v_x(x, 0) = \frac{\bar{\kappa}\bar{y}}{\pi(x^2 + \bar{y}^2)}. \quad (6)$$

The filaments are migrating in the same direction at a slower velocity,

$$v_x = \frac{\bar{\kappa}}{4\pi\bar{y}}, \quad (7)$$

which we will ignore in the following integral estimates. This overall migration velocity can be important when a series of pulses is being considered. In that case a quasi-steady state develops in which the systematic migration of the integrated vorticity entrains cold fluid stochastically at the edges of the hot channel.

To estimate the mixing time, we use Eq. (6) to calculate the time required for a fluid element starting at $x = -S_0$ to reach $x = S_0$, ignoring the effects of small scale turbulence. The equation of motion for this element is

$$\frac{dx}{dt} = v_x(x, 0) = \frac{\bar{\kappa}\bar{y}}{\pi(x^2 + \bar{y}^2)}, \quad (8)$$

which can be integrated to give

$$\int_0^\tau dt \equiv \tau_{\text{mix}} = \frac{\pi}{|\bar{\kappa}|\bar{y}} \int_{-S_0}^{S_0} dx (x^2 + \bar{y}^2). \quad (9)$$

The quadrature can be performed and gives the following mixing time estimate:

$$\tau_{\text{mix}} = \frac{2\pi S_0}{|\bar{\kappa}|\bar{y}} \left[\frac{S_0^2}{3} + \bar{y}^2 \right], \quad (10a)$$

where the vortex strength $\bar{\kappa}$ is given by Eq. (3) and the "average" displacement of this vorticity above the $y = 0$ plane is given formally by Eq. (5). Recently we have found that τ_{mix} has a simpler and perhaps more realistic interpretation. If we define V_0 to be the volume of the channel just after pressure equilibrium, τ_{mix} is approximately the time interval required for a volume V_0 of cool ambient air to mix with the hot channel gas. For an ideal gas, therefore, τ_{mix} is approximately the time in which the channel volume doubles.⁶

We note in Fig. 2 that, for the case of the elliptical channel (asymmetry class 2), two vortex filament pairs are generated and the flow is inward along the semimajor axes, a_x , and outward along the

semiminor axes, b_e . A representative τ_{mix} (and volume doubling time) can then be taken as the sum of the time intervals required for a fluid element to traverse half the ellipse along a_e and b_e respectively. For these times and each vortex filament pair, the derivation of Eq. (10a) will carry over directly. For the inward flow along the semimajor axis, a_e , we integrate from 0 to a_e for the fluid particle path rather than $-S_0$ to S_0 . In Fig. 2, the vortex filament pair most influencing this motion is that appearing on the right side of the minor axis. The displacement of these filaments is $2\bar{y} \approx 2b_e$. This gives us

$$\tau_{\text{mix}(a)} = \frac{\pi a_e}{|\bar{\kappa}_{2z}| \bar{y}} \left(\frac{a_e^2}{3} + \bar{y}^2 \right) \approx \frac{\pi a_e}{|\bar{\kappa}_{2z}| b_e} \left(\frac{a_e^2}{3} + b_e^2 \right). \quad (10b)$$

Similarly, for a fluid element traveling along the semiminor axis from $y = 0$ to b_e , the vortex filaments most influencing the motion are the two in the upper half plane and are therefore displaced by $2\bar{x} \approx 2a_e$; so we have

$$\tau_{\text{mix}(b)} \approx \frac{\pi b_e}{|\bar{\kappa}_{2z}| a_e} \left(\frac{b_e^2}{3} + a_e^2 \right). \quad (10c)$$

Our representative time scale would then be the sum of Eqs. (10b) and (10c),

$$\tau_{\text{mix}(2)} = \tau_{\text{mix}(a)} + \tau_{\text{mix}(b)} \quad (10d)$$

The case of three-dimensional distortions is more complex than the others, since two components ($\bar{\kappa}_{3z}$ and $\bar{\kappa}_{3\theta}$) of the residual vorticity are nonnegligible and are functions of z and θ , respectively. From Fig. 3, we see that for a given value of z , $\bar{\kappa}_{3z}$ is computed by assuming that the density distribution is offset from the pressure distribution, as for asymmetry class 1. The equation for $\tau_{\text{mix}(z)}$ is therefore identical to Eq. (10a) with $\bar{\kappa}$ as a function of z . We will find that the dependence on z leads to localization of the vorticity at $z = 0, \lambda/2$, and λ , in contrast to the case of off center beam propagation. Similarly we will find that $|\bar{\kappa}_{3\theta}|$ is largest when $\theta = 0^\circ$ or 180° , so that we can compute $\tau_{\text{mix}(\theta)}$ as the time for a fluid element to travel half a wavelength (for a sinusoidally curved channel) under the influence of vortex filaments of strength $|\bar{\kappa}_{3\theta}(0^\circ)| = |\bar{\kappa}_{3\theta}(180^\circ)|$. With a separation $2\bar{x} \approx 2R_1$, where R_1 is the radius of the channel cross section at pressure equilibrium we obtain

$$\tau_{\text{mix}(\theta)} \approx \frac{\pi \lambda}{2R_1 |\bar{\kappa}_{3\theta}(0)|} \left(\frac{\lambda^2}{12} + R_1^2 \right). \quad (10e)$$

While Eqs. (10a) and (10e) will give us an estimate of the mixing rate for asymmetry class three, we can define a channel doubling time only by computing the flux of ambient air into the channel under the influence of the total velocity field defined by the strengths $\bar{\kappa}_{3z}(z)$ and $\bar{\kappa}_{3\theta}(\theta)$.

C. Estimates of τ_{mix} from Dimensional Analysis

We may now use Eq. (10a) to estimate τ_{mix} for the first asymmetry class, in which a pulse is not collinear with a preformed hot channel. To do so, we require values for $\bar{\kappa}$ and \bar{y} . The remainder of this paper deals with the analytic calculation and numerical calibration of expressions for $\bar{\kappa}$. We will find a reasonable value for \bar{y} from the numerical simulation of sample problems. A simple dimensional analysis allows us to make at least crude estimates rather directly for the example of two successive, noncollinear pulses. A number of size scales enter the problem: S_0 , the radius of the channel created by the first pulse; the characteristic scale lengths for the pressure and density gradients; and the initial and final radii R_0 and R_1 of the second, displaced channel being formed. Fortunately most of the scales are either unimportant or expressible in terms of S_0 . If the first and second pulse have similar initial overpressures, R_1 and S_0 will be roughly equal and R_0 will be a modest fraction of R_1 . Our numerical simulations (Section V) support the approximate equality of S_0 and R_1 .

We expect other simplifications. Whether a shock expansion or an adiabatic expansion is being driven by energy deposition, the larger the pressure gradient the smaller the time over which it acts. Thus the integrated vorticity is relatively insensitive to the shock thickness. Similarly, the density gradient is integrated over space so the inner and outer densities (ρ_0 and ρ_∞) enter, but the scale length of the transition region can be neglected. We expect and will in fact show that the maximum vorticity generation occurs when $X_0 \approx S_0$. Thus there are no small parameters arising as ratios of characteristic lengths unless we consider exceptionally tightly focused pulses, in which case $R_0 \ll R_1 \approx S_0$, or only slight departures from the symmetric superposition of the pulses, in which case $X_0 \ll S_0$.

The integrated vorticity $\bar{\kappa}$ has units of cm^2/sec , a length times a velocity or a characteristic time multiplied by a velocity squared. The characteristic velocity will be the expansion velocity. When the energy deposition is fast and the pulses are strong, this velocity is a characteristic sound speed c_s . The characteristic time is the expansion duration (if the energy deposition is slow) or the sonic transit time S_0/c_s . Thus we expect

$$\bar{\kappa}_{1z} = c_s S_0 F_{1z} \quad (11)$$

where F_{1z} is a dimensionless form factor containing geometric effects, detailed hydrodynamic interactions, and information about the channel and beam profiles. Cancellation effects, leaving $\underline{v} \cdot \underline{\nabla} \underline{v}$ as the

dominant contribution to the vorticity source term, generally reduce F_{12} somewhat below unity. We will demonstrate this in Section IV.

If we assume that $\bar{v} \approx 0.8S_0$, Eq. (10) for the mixing time becomes

$$\tau_{\text{mix}} \approx 7.9S_0/(c_s F_{12}). \quad (12)$$

For a strong pulse which heats the gas appreciably on passage, we shall assume $F_{12} \approx 0.5$. Taking 5×10^4 cm/s as a generic value for c_s and choosing $S_0 = 1$ cm gives $\tau_{\text{mix}} \approx 300 \mu\text{s}$. This time scale is at least three orders of magnitude shorter than that of classical thermal conduction.⁵

If we consider only the large scale convective flows, this 300 μs "mixing time" from the dimensional analysis estimate of Eq. (10a) is the time for cold material from one side of a hot channel to cross the channel and reach the other side. Because of the presence of small scale turbulence and other perturbations which can affect the interaction of the vortex filaments, the fluid particles will be likely to follow a more random path inside the channel. In addition, true mixing of hot and cold fluid will probably take somewhat longer because one or two rotations of the vortices will be required to entrain and smear in an appreciable amount of the cooler fluid. This "mixing" time, however best defined, is clearly important when comparable to or less than the time interval between pulses.

In the next section, we perform an integration of the vorticity source term in Eq. (1) to improve on Eqs. (11) and (12), our dimensional analysis estimates. Using a few reasonable assumptions, we obtain a quadrature for the integrated vorticity $\bar{\kappa}_{1a}$, which will display the various nondimensional dependences of the form factor F_{1a} .

IV. APPROXIMATE VORTICITY INTEGRALS

Equation (3) defines the residual vortex strength following expansion to pressure equilibrium ($t > \tau$) and will be evaluated analytically to replace Eq. (11) in the mixing time estimates, Eqs. (10). First, however, we must integrate Eq. (1) over the time interval $(0, \tau)$. We begin by stating several assumptions which will permit us to perform these integrals.

We model the deposition of energy as instantaneous and use pressure pulses of finite size with an appropriate radial profile and a total energy which is equivalent to that of the laser pulses or electric discharges. This is a reasonable assumption for the experiments of Greig et al.,¹⁻⁵ in which the discharges were much shorter in duration than the expansion times of the hot channels. Our model deposits the energy as internal energy only, and we, therefore, do not consider relaxation of excited molecular and atomic states. The presence of long-lived states will slow expansion of the channel.

however, our analytic model becomes more accurate in this case, as discussed below. The variable $R(t)$ will denote the radius of an expanding cylinder of hot gas which is produced by the latest pulse. Note that, according to Section III.B, $R(0) = R_0$ and $R(\tau) = R_1$. To represent the flow field of the expanding channel, we assume that the flow in the outside region ($r > R(t)$) behaves incompressibly and the inside, beam-heated region expands uniformly. Thus

$$v_r(r, t) = \begin{cases} rU(t)/R(t) & \text{if } r \leq R(t) \\ U(t) R(t)/r & \text{if } r > R(t) \end{cases} \quad (13)$$

specifies the flow everywhere as a function of the heated region radius $R(t)$ and velocity $U(t) \equiv \dot{R}(t)$. This flow has a uniform but time varying divergence inside the heated region and zero divergence outside. In reality the fluid inside the just-heated channel will give up energy to the cold surrounding fluid via shocks, and a fraction of the pulse-deposited energy will even escape to infinity as an acoustic wave. The smooth shape of the expanded channels observed from 1D hole-boring calculations⁷ and the computational and experimental⁵ result that most of the deposited energy stays close to the original pulse deposition region support the approximations implied by using the flow field, Eq. (13). We note that Eq. (13) becomes a better representation as the rate of energy deposition decreases.

As we will soon show more explicitly, the important feature of vorticity generation is the radial distance which each fluid element moves. Pressure gradients arising from accelerations of a fluid element do not really contribute to vorticity in the present context. Because the fluid elements begin and end their expansion-induced displacement at rest, the average acceleration is zero. The $\underline{v} \cdot \nabla \underline{v}$ vorticity source term has the same sign throughout the expansion and consequently contributes more strongly to the integrated vorticity.

Because our velocity field during expansion is radial and varies only with r , the coupling term $\underline{\xi} \cdot \nabla \underline{v}$ in Eq. (1) is initially negligible. Further, the maximum vortex induced flow speed which resides in the system is much smaller than the maximum expansion speed. This term, therefore remains small relative to the other terms throughout the expansion and may be neglected. To evaluate the pressure gradient in the source term we may use the flow field, Eq. (13), in the equation of motion to obtain

$$-\frac{1}{\rho} \nabla_r P = \frac{dv_r}{dt} = \begin{cases} r \frac{d}{dt} (U/R) + r U^2/R^2 & \text{if } r \leq R(t) \\ \frac{1}{r} \frac{d}{dt} (UR) - U^2 R^2/r^3 & \text{if } r > R(t) \end{cases} \quad (14)$$

Notice that we assume that the acceleration in the radial direction has values strictly appropriate only when feedback of the asymmetric density gradients on the driving expansion flow are small. The model appears to work quite well for large density variations as well, a result that is understandable in hindsight. The maximum vortex-induced flow speed which resides in the system is much smaller than the maximum expansion speed. Further, the vorticity is generated essentially instantaneously relative to the mixing timescale τ_{mix} . Thus the generation term can be calculated assuming that the asymmetric density gradients do not change the expansion-driven pressure gradients and that the vorticity which develops does not affect the density gradients during the relatively brief expansion.

Since the pressure gradients are assumed to be radial, the radial vorticity component will be negligible and we need to evaluate only the azimuthal and axial gradients of the density. Our representation of the density profile is

$$\rho(\underline{s}, t) = \rho_{\infty} \exp[-\ln(\rho_{\infty}/\rho_0) g(\underline{s}, S_0, t)] \quad (15)$$

where $g(0, S_0, 0) = 1$; $g(\infty, S_0, 0) = 0$; \underline{s} is a displacement vector; and S_0 is a characteristic scale length defined in Figs. 1-3. Normally $g(\underline{s}, S_0, t)$ is a function of the ratio \underline{s}/S_0 . In the subsections below, we will evaluate $\bar{\kappa}_{1\alpha}$ for the three general asymmetry classes. For brevity we will discuss the off center beam propagation case in detail and shorten the presentation for the other two cases.

A. Off Center Beam Propagation

As indicated by Fig. 1, the case of off center beam propagation is two-dimensional, and the dominant contribution is the passage of the shock across the preformed hot channel, which is assumed to be cylindrical. Thus we may use the flow field at and outside of the boundary of the expanding channel ($r \geq R(t)$). Because the problem is two-dimensional, \underline{v} , ρ , and P do not vary with z , and for this reason, only ξ_z is nonzero. Noting that the flow field in the outer region is incompressible and using Eqs. (1), (14), and (15), we have for

$$\frac{d\xi_z}{dt} = \begin{cases} \approx 0 & \text{if } r < R(t) \\ \ln\left(\frac{\rho_{\infty}}{\rho_0}\right) \frac{\partial g(\underline{s})}{\partial \theta} \left[\frac{(UR)^2}{r^4} - \frac{1}{r^2} \frac{d}{dt}(UR) \right] & \text{if } r \geq R(t) \end{cases} \quad (16)$$

Because we assume that the vorticity does not affect the density gradients during the relatively brief expansion, $g(\underline{s})$ does not vary with time in our model, and, therefore, describes the channel prior to deposition of the latest pulse. Notice that we have suppressed S_0 as an argument of $g(\underline{s})$. We will take S_0 into account when evaluating form factors later in this section. We may now calculate $\bar{\kappa}_{1z}$ by

using Eq. (16) in Eq. (3). Since we are currently using Eulerian variables, we may reverse the order of the time and spatial integrations to obtain

$$\begin{aligned} \bar{\kappa}_{1z}(\tau) = \ln(\rho_\infty/\rho_0) \int_0^\tau dt \int_0^\pi d\theta \int_{R(t)}^\infty dr r \frac{\partial g(s)}{\partial \theta} \\ \times \left[\frac{(UR)^2}{r^4} - \frac{1}{r^2} \frac{d(UR)}{dt} \right]. \end{aligned} \quad (17)$$

We now change to the Lagrangian variables (r_0, θ_0) where

$$\begin{aligned} r \rightarrow r(t) = \sqrt{r_0^2 + R^2(t) - R_0^2} \\ \theta = \theta_0. \end{aligned} \quad (18)$$

This gives us

$$r dr = r_0 dr_0, \quad (19)$$

and $r(t)$ is the instantaneous radial position of a fluid element initially at $r(0) \equiv r_0$. In terms of r_0 , the radial density variable s becomes

$$s = (X_0^2 + r_0^2 - 2X_0r_0 \cos \theta)^{1/2} \quad (20)$$

and the integral in Eq. (17) can be performed without approximation. This gives us

$$\int_0^\pi d\theta \frac{\partial g}{\partial \theta} = \begin{cases} g(r_0 + X_0) - g(X_0 - r_0), & r_0 \leq X_0 \\ g(r_0 + X_0) - g(r_0 - X_0), & r_0 > X_0 \end{cases} \quad (21)$$

and Eq. (17) becomes

$$\begin{aligned} \bar{\kappa}_{1z}(\tau) = \ln\left(\frac{\rho_\infty}{\rho_0}\right) \int_0^\tau dt \cdot \\ \times \left\{ \int_{R_0}^\infty \frac{dr_0 r_0}{r^2(t)} g(r_0 + X_0) \left[\frac{(UR)^2}{r^2(t)} - \frac{d(UR)}{dt} \right] \right. \\ - \int_{R_0}^{X_0} \frac{dr_0 r_0}{r^2(t)} g(X_0 - r_0) \left[\frac{(UR)^2}{r^2(t)} - \frac{d(UR)}{dt} \right] \\ \left. - \int_{X_0}^\infty \frac{dr_0 r_0}{r^2(t)} g(r_0 - X_0) \left[\frac{(UR)^2}{r^2(t)} - \frac{d(UR)}{dt} \right] \right\}. \end{aligned} \quad (22)$$

Notice that the expression in Eq. (22) is long because of the requirement that the radial variable s be positive or zero. Equation (21) is necessary, for instance, when $g(\underline{s}, S_0)$ is a square well

$$g(\underline{s}, S_0) = \begin{cases} 1, & s \leq S_0 \\ 0, & s > S_0 \end{cases} \quad (23)$$

which is not defined for negative s . However, if $g(\underline{s}, S_0)$ is an even function of s , such as a Gaussian, then Eq. (21) represents an irrelevant distinction and Eq. (22) shortens considerably.

The integral in Eq. (22) is difficult to perform even if $R(t)$ for our particular case is known, and further approximations must be made to get a usable analytic result. The approximation most useful is to evaluate the integrand at a specific time. If we assume that the initial and final states of the expansion are at rest, we have $U(0) = U(\tau) = 0$. The expansion flux $R(t)U(t)$ will then peak at a time $0 < t_m < \tau$. We will evaluate the integrand in terms of t_m . If the function $R(t)U(t)$ is approximately symmetric about $t = t_m$, a reasonable approximation for the term $U^2(t)R^2(t)$ in Eq. (22) would be half the maximum value, i.e.,

$$U^2(t)R^2(t) \approx U^2(t_m)R^2(t_m)/2 \equiv U_m^2 R_m^2/2. \quad (24)$$

We also replace $r(t)$ by $r_m = \sqrt{r_0^2 + R_m^2 - R_0^2}$. Because r_m does not vary with time and because the system is at rest at $t = 0$ and $t = \tau$, the term proportional to $\frac{d(UR)}{dt}$ integrates to zero. This term, therefore, corresponds to a transient in the vorticity during the expansion to pressure equilibrium. As the time approaches $t = \tau$, we expect the vorticity strength to approach a value which will be approximately constant for $t > \tau$. With the above simplifications, we may perform the time integration of Eq. (22) to obtain

$$\begin{aligned} \bar{\kappa}_{1z}(\tau) \approx & \frac{U_m^2 \tau}{2} \ln \left[\frac{\rho_\infty}{\rho_0} \right] \left\{ \int_{R_0}^{\infty} dr_0 r_0 \frac{R_m^2 g(r_0 + X_0)}{(r_0^2 + R_m^2 - R_0^2)^2} \right. \\ & \left. - \int_{R_0}^{X_0} dr_0 r_0 \frac{R_m^2 g(X_0 - r_0)}{(r_0^2 + R_m^2 - R_0^2)^2} - \int_{X_0}^{\infty} dr_0 r_0 \frac{R_m^2 g(r_0 - X_0)}{(r_0^2 + R_m^2 - R_0^2)^2} \right\} \end{aligned} \quad (25)$$

for the residual vorticity. We may approximate the expansion time τ by

$$\tau \approx 2(R_1 - R_0)/U_m \quad (26)$$

where, as before, $R_0 = R(0)$ and $R_1 = R(\tau)$. In Eq. (26), we use $U_m/2$ to estimate the average velocity of expansion.

Next we write the integral in terms of three nondimensional parameters

$$\begin{aligned} a &\equiv R_w/R_m < 1, \\ b &\equiv R_m/S_0 \leq 1, \\ c &\equiv X_0/S \approx 1. \end{aligned} \quad (27)$$

Letting the integration variable be $\eta \equiv r/R_m$ yields

$$\begin{aligned} \bar{\kappa}_{1z}(\tau) = \frac{U_m^2 \tau}{2} \ln \left(\frac{\rho_\infty}{\rho_0} \right) &\left\{ \int_a^\infty d\eta \, \eta \frac{g(S_0[\eta b + c])}{(1 + \eta^2 - a^2)^2} \right. \\ &\left. - \int_a^{c/b} d\eta \, \eta \frac{g(S_0[c - \eta b])}{(1 + \eta^2 - a^2)^2} - \int_{c/b}^\infty d\eta \, \eta \frac{g(S_0[\eta b - c])}{(1 + \eta^2 - a^2)^2} \right\}. \end{aligned} \quad (28)$$

If the remaining composite integral is identified as a three parameter form factor $f_{1z}(a, b, c)$ with values of order unity, the very useful improvement on the dimensional approximation (Eq. (11)) is obtained:

$$\begin{aligned} \bar{\kappa}_{1z}(\tau) &\approx (U_m^2 \tau / 2) \ln(\rho_\infty / \rho_0) f_{1z}(a, b, c) \\ &\approx U_m (R_1 - R_0) \ln(\rho_\infty / \rho_0) f_{1z}(a, b, c). \end{aligned} \quad (29)$$

Here the form factor f_{1z} is generally less than 1/2. The sign of f_{1z} indicates the direction of flow in the (x, y) plane—counterclockwise or clockwise.

We will now include the explicit dependence of the function $g(s, S_0)$ upon S_0 ; usually this occurs as the ratio s/S_0 . In this case, the multiplicative S_0 in Eq. (28) will cancel with that in the denominator. For this reason, the form factor f_{1z} in Eq. (29) depends only on the ratios a , b , and c , and not explicitly on S_0 , and we have

$$\begin{aligned} f_{1z}(a, b, c) = \int_a^\infty d\eta \, \eta \frac{g(\eta b + c)}{(1 + \eta^2 - a^2)^2} &- \int_a^{c/b} d\eta \, \eta \frac{g(c - \eta b)}{(1 + \eta^2 - a^2)^2} \\ &- \int_{c/b}^\infty d\eta \, \eta \frac{g(\eta b - c)}{(1 + \eta^2 - a^2)^2}. \end{aligned} \quad (30)$$

The general integral form factor, Eq. (30), can be evaluated numerically for any reasonable profile $g(s/S_0)$. Figure 5 shows plots of f_{1z} versus c , the measure of channel separation, for several values of

a at $b = 0.7$ and for several values of b at $a = 0.6$. These values are close to the actual initial conditions for the detailed calculation of the next section. In this figure the super-Gaussian density profile was used,

$$g_{SG}(s/S_0) = \exp(-s^2/S_0^2) \quad (31)$$

and the integrations were performed using a numerical quadrature algorithm. We have also evaluated f_{12} for a Bennett profile,

$$g_B(s/S_0) = -\ln \left[1 - \frac{\rho_\infty - \rho_0}{\rho_\infty (1 + s^2/S_0^2)^2} \right] / \ln(\rho_\infty/\rho_0); \quad (32)$$

the results appear in Fig. 6. In Eq. (32), the "Bennett radius" is equal to S_0 . In the case of a square well density discontinuity at $s = S_0$, Eq. (23), the integral can be performed analytically to give

$$f_{12}^{sw}(a, b, c) = \frac{1}{2} \left[\frac{b^2}{(1+c)^2 + b^2(1-a^2)} - \frac{b^2}{(1-c)^2 + b^2(1-a^2)} \right] \quad (33)$$

for $c > 1 + ab$. This is the case when the second pulse is wholly outside the channel formed by the first pulse. As c approaches ∞ , f_{12}^{sw} decreases as $-1/c^3$; so pulse channels separated by more than 3 radii interact only weakly.

When the channels are closer, we have $c \leq 1 + ab$, and the channels overlap somewhat. As long as $c > 1 - ab$ there is still part of the second channel of initial radius R_0 outside the cylinder $s = S_0$. For this region of values, $1 - ab < c \leq 1 + ab$, we have

$$f_{12}^{sw}(a, b, c) = \frac{1}{2} \left[\frac{b^2}{(1+c)^2 + b^2(1-a^2)} - 1 \right] \quad (34)$$

Equation (34) agrees with Eq. (33) at the interfacial separation $c = 1 + ab$.

There is a third region where the initial radius of the second channel lies wholly within the first, i.e., $c \leq 1 - ab$. Then $f_{12}^{sw}(a, b, c)$ satisfies Eq. (33) again. In the intermediate region $1 - ab \leq c \leq 1 + ab$, f_{12}^{sw} takes on its lowest negative value at the exterior touching point $c = 1 + ab$. For larger values of c the magnitude $|f_{12}^{sw}|$ decreases and for smaller values $|f_{12}^{sw}|$ decreases monotonically to zero at $c = 0$. This lowest negative value is

$$\left(f_{12}^{sw} \right)_{\min} = - |f_{12}^{sw}|_{\max} = \frac{-2(1+ab)}{(4+4ab+b^2)} \quad (35)$$

When $ab = b^2 = 1/2$, $|f_{12}^{sw}|_{\max} = 6/13$, which is close to the values in Figs. 5 and 6 for f_{12}^{SG} and f_{12}^B , respectively.

Also of interest is the slope $\frac{\partial f}{\partial c}$ at $c = 0$, where the pulses are concentric and no vorticity generation is expected.

$$\left. \frac{\partial f_{1z}^*}{\partial c} \right|_{c=0} = \frac{-2b^2}{[1 + b^2(1 - a^2)]^2}, \quad (36)$$

which is nonzero and large. Thus even modest nonconcentricity leads to appreciable vorticity and mixing. Similar behavior is observed in the two smooth profiles considered as well. Figure 7 compares f_{1z}^B , f_{1z}^{SG} , and f_{1z}^* for $a = b = 1/\sqrt{2}$ to demonstrate the similarity of the vorticity generation form factors regardless of the profile. This relative profile insensitivity arises because $\bar{\kappa}_{1z}$ is an integral quantity, the total upper half plane circulation.

Returning to our integrated vorticity estimate of Eq. (29) with a maximum form factor of 6/13, and $U_m \approx c_s$ we have

$$|\bar{\kappa}_{1z}|_{\max} \approx \frac{6}{13} c_s (R_1 - R_0) \ln \left(\frac{\rho_\infty}{\rho_0} \right). \quad (37)$$

Using Eq. (8) and assuming $\bar{y} \approx R_1 - R_0$ gives an estimate for the maximum velocity on the x-axis:

$$|v_x|_{\max} \approx \frac{6}{13\pi} \ln \left(\frac{\rho_\infty}{\rho_0} \right) c_s. \quad (38)$$

Under optimum conditions the velocity between the vortex filaments approaches a quarter of the sound speed in the surrounding fluid. When the expansion is subsonic throughout (where this analysis ought to be most accurate), c_s in Eq. (38) should be replaced by the appropriately averaged expansion velocity U_m .

Using Eq. (10a) for the mixing time with $\bar{y} \approx 0.8S_0 \approx R_1 - R_0$ and $\bar{\kappa}_{1z}$ Eq. (37) above gives

$$(\tau_{mix})_{\min} \approx \frac{6.8\pi S_0}{c_s \ln \left(\frac{\rho_\infty}{\rho_0} \right)}. \quad (39)$$

With $c_s \approx 5 \times 10^4$ cm/s, $\ln(\rho_\infty/\rho_0) \approx 2.5$, and $S_0 = 1.0$ cm, the fastest mixing time is about 170 μ s. This estimated fastest mixing time is within a factor of two of the dimensional estimate. In any particular system the integral of Eq. (30) can be performed numerically and the resulting form factor substituted into Eq. (29) for the integrated vorticity.

The sign of $\bar{\kappa}_{1z}$ is negative for the configuration of Fig. 1 where the second pulse is centered to the left of the original channel. This means that the jet of colder gas across the original channel starts

on the side opposite to the displaced second pulse and rushes toward the newly heated region. On average the old channel moves toward the new channel. This average motion does not imply mixing but the spatial behavior of the flow from the vortex filament pair, as will be seen in the simulations of Section V (Fig. 16), effectively bisects the composite hot channel with a cold jet. The result is two smaller channels above and below the original symmetry plane in which the vortex filaments are now centered. A third pulse located at $y = 0$ between the two modified channels will cause each of these smaller channels to bifurcate again with fluid jets from the top of the upper channels and the bottom of the channel impinging on the third expanding channel from above and below.

B. Two-Dimensional Distortion (Elliptical Channel)

The above results are readily generalizable to the other symmetry classes, and we, therefore, will not evaluate the form factors in detail as we have done above. To illustrate the effect of smooth distortions of a pulse (envelope) from a circular cross section, we will treat the expansion of an elliptical pulse. By smooth distortions, we mean in this example that all of the pressure and density contours of the pulse will be elliptical in shape. For a Bennett profile, we may express this as

$$P(x, y) = P_{\infty} + \frac{P_0 - P_{\infty}}{\left\{ 1 + \frac{[(x - x_0)^2/\beta + \beta(y - y_0)^2]}{R_0^2} \right\}^2} \quad (40)$$

In Eq. (40), $R_0^2 = a_e b_e$, where a_e and b_e are the semimajor and semiminor axes of the elliptical envelope of the pulse, and $\beta = a_e/b_e$.

Initially the pressure and density gradients will be approximately parallel. As the channel expands, the density distribution will retain an elliptical shape while the pressure distribution and the flow pattern will approach radial symmetry. Consequently the source term in Eq. (1) will be nonzero when integrated over the expansion period τ . In contrast to the off center beam propagation case, the largest contribution to the vorticity comes from the flows in the interior of the expanding channel boundary ($r \leq R(t)$), since the density is relatively uniform outside. Our derivation will assume the configuration of Fig. 2, where the circle represents the pressure distribution and the ellipse forms the envelope of the density distribution. Since we will not account for the noncylindrical shape of the pressure distribution at early times, Eq. (13) provides an adequate description of the flow field for this model. The problem is two-dimensional, as in the case of the first asymmetry class; so only ξ_z is nonzero. The divergence of the flow velocity is nonzero, i.e.,

$$\nabla \cdot \mathbf{v} = \frac{2U}{R} \quad (41)$$

Because the vorticity generating flows are, therefore, compressible, the integration of Eq. (1) is simplest if we use Lagrangian variables from the beginning. The density of a fluid element will vary inversely with its volume over time, as determined by Eq. (41). We may express the average reduction in density as the channel expands by the equation⁸

$$\rho(\underline{r}, t) \approx \rho(\underline{r}, 0) R_0^3 / R^3(t) \quad (42)$$

where \underline{r} now varies with time, $R(t)$ is the boundary of the outward flow as in Eq. (13) and $R_0 = R(0)$. Using Eq. (42) and Eq. (15) with $r = 0$, we find that, to a very good approximation,

$$\frac{\partial}{\partial \theta} \ln \rho(\underline{r}, t) \approx \frac{\partial}{\partial \theta} \ln \rho(\underline{r}, 0) = -\ln(\rho_\infty / \rho_0) \frac{\partial}{\partial \theta} g(\underline{r}, 0). \quad (43)$$

As in Section IV.A, we have suppressed the dependence on S_0 and, in this case X_0 , to shorten our notation. Thus the density distribution at very early times dominates the density dependence of the source term. With Eqs. (14 and 41-43), Eq. (1) becomes

$$\frac{d\xi_z}{dt} + \frac{2U}{R}\xi_z = -\ln\left(\frac{\rho_\infty}{\rho_0}\right) \frac{\partial}{\partial \theta} g(\underline{r}, 0) \left[\frac{d}{dt} \left(\frac{U}{R} \right) + \frac{U^2}{R^2} \right]. \quad (44)$$

We may now integrate Eq. (44) over the time interval $(0, \tau)$. As in the case of the density, the vorticity present in a fluid element at time $t < \tau$ decreases with subsequent expansion by the factor $R^2(t)/R^2(\tau)$. This effect is associated with the nonzero divergence of the velocity and thus accounts for the second term on the left hand side of Eq. (44).

Our Lagrangian variables are $r(\tau)$ and $\theta(\tau) = \theta$ (constant in time), which give the position of a fluid element at time $t = \tau$. From Eq. (13) we find that $r(\tau)$ and $r(0) \equiv r_0$ are related by

$$r_0 = \frac{r(\tau)R_0}{R(\tau)}. \quad (45)$$

When we express the initial density distribution in terms of $r(\tau)$, the vorticity at time τ is the integral of the source term in Eq. (44) over the time interval $(0, \tau)$, reduced by the factor $R^2(t)/R^2(\tau)$ to account for the nonzero divergence of the velocity. This gives us

$$\begin{aligned} \xi_z(r, \theta, \tau) &\approx -\ln\left(\frac{\rho_\infty}{\rho_0}\right) \frac{\partial}{\partial \theta} g\left(\frac{r(\tau)R_0}{R(\tau)}, \theta\right) \int_0^\tau dt \frac{R^2(t)}{R^2(\tau)} \left[\frac{d}{dt} \left(\frac{U}{R} \right) + \frac{U^2}{R^2} \right] \\ &\approx -\frac{1}{R^2(t)} \ln\left(\frac{\rho_\infty}{\rho_0}\right) \frac{\partial}{\partial \theta} g\left(\frac{r(\tau)R_0}{R(\tau)}, \theta\right) \int_0^\tau dt \left[\frac{d}{dt} (UR) - U^2 \right]. \end{aligned} \quad (46)$$

Following the development of Section A, we note that the term $d(UR)/dt$ integrates to zero, and we approximate the remaining portion of the integral in terms of $t = t_m$, when the expansion flux $U(t) R(t)$ reaches a maximum. This gives us

$$\xi_z(r, \theta, \tau) \approx \frac{U_m^2 \tau}{2 R^2(\tau)} \ln \left(\frac{\rho_\infty}{\rho_0} \right) \frac{\partial}{\partial \theta} g \left(\frac{r(\tau) R_0}{R(\tau)}, \theta \right). \quad (47)$$

Comparing this with the results of Section A, we see that the form of $\bar{\kappa}_z$ will be quite similar in the two cases.

We may now integrate Eq. (47) over the quarter plane, which contains a single vortex filament, as shown in Fig. 2. The integral is

$$\bar{\kappa}_{2z} \approx \frac{U_m^2 \tau}{2 R^2} \ln \left(\frac{\rho_\infty}{\rho_0} \right) \int_0^{\pi/2} d\theta \int_0^\infty dr r \frac{\partial}{\partial \theta} g \left(\frac{r R_0}{R}, \theta \right) \quad (48)$$

where r and R are functions of τ . We may perform the θ integral and use Eq. (45) to transform from $r(\tau)$ to $\eta \equiv r/R_0$ as an integration variable. If we now include the explicit dependence on X_0 and S_0 we obtain

$$\begin{aligned} \bar{\kappa}_{2z} &\approx \frac{U_m^2 \tau}{2} \ln \left(\frac{\rho_\infty}{\rho_0} \right) f_{2z}(a, b, c) \\ &\approx U_m (R_1 - R_0) \ln \left(\frac{\rho_\infty}{\rho_0} \right) f_{2z}(a, b, c), \end{aligned} \quad (49)$$

where a , b , and c are given by Eq. (27). The form factor is

$$f_{2z}(a, b, c) = \int_0^\infty d\eta \eta \left[g(ab\eta, \frac{\pi}{2}, c) - g(ab\eta, 0, c) \right]. \quad (50)$$

For the initial effective radius of the flow field, we use $R_0^2 = a_e b_e$, in which a_e and b_e are the semimajor and semiminor axes of the pressure pulse.

We may calculate the form factor f_{2z} for a super-Gaussian density distribution,

$$g \left(\frac{r_0}{S_0}, \theta, \frac{X_0}{S_0} \right) = \exp \left[- \left(\frac{r_0}{S_0} \frac{1}{1 + \left(\frac{X_0}{S_0} \right) \cos 2\theta} \right)^2 \right]. \quad (51)$$

Inserting Eq. (51) into Eq. (50), we have

$$f_{2z} = - \frac{2X_0 S_0}{R_0^2} \quad (52)$$

For $S_0 \approx R_0$ and $X_0 \approx 1/2 S_0$, $|f_{2z}| \approx 1$, and our form factor is a factor of ~ 2 larger than for asymmetry class one. However, since we did not account for the approximate alignment of the pressure and density at early times, we might expect $|f_{2z}|$, as given by Eq. (50), to be too large by a similar factor. Thus, we would expect a more exact calculation of $|f_{2z}|$ to yield values similar to those of $|f_{1z}|$.

C. Three-Dimensional Distortions

A pulse may also have an axis which is curved or kinked. This curvature may be the result of a perturbation in the envelope of the pulse, as in the case of a deformable solid, or alternatively, could occur if the deposition of energy along the axis is nonuniform. Our current treatment assumes the former case, in which the pulse is deformed smoothly, and we will consequently parallel Section IV.B in our general approach. Figure 3 shows that we choose the z -axis to coincide with the center of mass of the pulse. This causes the density to vary as a function of z and θ , and both ξ_z and ξ_θ are nonnegligible. We will discuss each component separately, taking ξ_z first.

C.1 Derivation of $\bar{\kappa}_{3z}$

The assumptions of Section IV.B apply directly to the derivation of $\bar{\kappa}_{3z}$, since the interior flows are again responsible for the vorticity generation. Figure 3 indicates that the flow is radial from the z axis, and R_0 , the radius of the expansion wave, is $\geq |X_0| S_0$, where X_0 is the displacement of the channel axis from the z -axis. By convention X_0 will be positive for a displacement of the channel to the right of the z -axis. The situation resembles the first asymmetry class, off-center beam propagation, although X_0 oscillates between positive and negative values as z changes. As in Section IV.B, we initially suppress z , X_0 , and S_0 in our argument list for $g(s, r)$. Carrying over Eqs. (41)-(47), we find that

$$\bar{\kappa}_{3z}(z, \tau) \approx \frac{U_m^2 \tau}{2R^2} \ln \left(\frac{\rho_\infty}{\rho_0} \right) \int_0^\pi d\theta \int_0^\infty dr r \frac{\partial}{\partial \theta} g \left(s \left[\frac{rR_0}{R}, \theta \right] \right) \quad (53)$$

in which r and R are functions of τ . Because of the similarity to asymmetry class one, we see that the radial variable s is given by Eq. (20) with X_0 a function z , and the θ integral is given by Eq. (21). We may now transform our radial integration variable from $r(\tau)$ to $\eta = r_0/R_0$, as was done in solving Eq. (48) for asymmetry class two. This gives us

$$\bar{\kappa}_{3z}(z, \tau) \approx \frac{U_m^2 \tau}{2} \ln \left(\frac{\rho_\infty}{\rho_0} \right) f_{3z}(a, b, c, z) \quad (54)$$

where the dependence on $X_0(z)$ and S_0 is now explicitly included through the ratios a , b , and c , which are defined in Eq. (27). With the assumption that $g(\underline{s}, S_0) = g(\underline{s}/S_0)$, the form factor is

$$f_{3z}(a, b, c, z) = \int_0^\infty d\eta \, \eta \, g(ab\eta + c, z) - \int_0^{c/ab} d\eta \, \eta \, g(c - ab\eta, z) - \int_{c/ab}^\infty d\eta \, \eta \, g(ab\eta - c, z). \quad (55)$$

As an example let us use a Gaussian function for $g(\underline{s}/S_0)$, Eq. (31), where s is given by Eq. (20) with

$$X_0(z) = h \cos(2\pi z/\lambda) \quad (56)$$

in the coordinate system defined by Fig. 3. Equation (55) gives us

$$f_{3z} = -\sqrt{\pi} \frac{X_0(z) S_0}{R_0^2}. \quad (57)$$

Note the similarity with our calculation for f_{2z} (Eq. (52)). We also pointed out earlier in this subsection and in Fig. 3 that, in our model for the flow field, $R_0 \leq |X_0| + S_0$, and, therefore, suggest using $h + S_0$ as an estimate for R_0 . If $h \approx S_0$, then the average magnitude of X_0 is $\approx 2/3 S_0$ and we find that the average $|f_{3z}|$ is ≈ 0.3 . As for the elliptical channel case, the pressure will not be symmetric about the z -axis at early times, and our values for $|f_{3z}|$ may be somewhat high. Note that, by Eq. (56), most of the vorticity is generated at the ends and center of the channel section.

C.2. Derivation of $\bar{\kappa}_{3\theta}$

To solve for the θ component of the vortex filament strength, we return to Eq. (1). Following the line of reasoning which lead to Eq. (44), we find that

$$\frac{d\xi_\theta}{dt} + \frac{2U}{R} \xi_\theta = \ln \left(\frac{\rho_\infty}{\rho_0} \right) \left[\frac{\partial g}{\partial z} \right] r \left[\frac{d}{dt} \left(\frac{U}{R} \right) + \frac{U^2}{R^2} \right]. \quad (58)$$

Again the density distribution at early times determines the vorticity through the derivative of $g(\underline{s}, S_0, 0)$ in Eq. (58). Proceeding as in subsections IV.B and C.1, we use Lagrangian variables $r(t)$, θ , and z , and integrate over time first to obtain

$$\xi_\theta(r, \theta, z, \tau) \approx \frac{1}{R^2(\tau)} \ln \left(\frac{\rho_\infty}{\rho_0} \right) \frac{\partial}{\partial z} g \left[s \left[\frac{r(\tau) R_0}{R(\tau)}, \theta, z \right] \int_0^\tau dt \, r(t) \left[\frac{d}{dt} (UR) - U^2 \right] \right]. \quad (59)$$

As in the case of Eq. (22), we simplify our integral by replacing $r(t)$ with the value of r at a specific time; here we use $r(\tau)$, which is the most convenient choice for the spatial integral below. Again we note that $d(UR)/dt$ integrates to zero, and we approximate the remaining portion of the integral in terms of $t = t_m$. Thus we obtain

$$\xi_{3\theta}(r, \theta, z, \tau) \approx - \frac{U_m^2 \tau}{2R^2(\tau)} \ln \left(\frac{\rho_\infty}{\rho_0} \right) r(\tau) \frac{\partial}{\partial z} g \left[s \left[\frac{r(\tau)R_0}{R(\tau)}, \theta, z \right] \right]. \quad (60)$$

We now integrate Eq. (60) over the region $\{r \in (0, \infty), z \in (0, \lambda/2)\}$, which contains vorticity of one sign, in analogy to the two-dimensional cases. The integral is

$$\bar{\kappa}_{3\theta} \approx - \frac{U_m^2 \tau}{2R^2(\tau)} \ln \left(\frac{\rho_\infty}{\rho_0} \right) \int_0^\infty dr r \int_0^{\lambda/2} dz \frac{\partial}{\partial z} g \left[s \left[\frac{r(\tau)R_0}{R(\tau)}, \theta, z \right] \right]. \quad (61)$$

We now perform the z integral and use Eq. (45) to transform $r(\tau)$ to $\eta \equiv r_0/R_0$ as an integration variable. Including the explicit dependence on X_0 and S_0 through the ratios r_0/S_0 and X_0/S_0 as before, we have

$$\bar{\kappa}_{3\theta}(\tau, \theta) \approx - \frac{U_m^2 \tau}{2} \ln \left(\frac{\rho_\infty}{\rho_0} \right) f(a, b, c, \theta) \quad (62)$$

where a , b , and c are defined by Eq. (27) and the form factor is

$$f_{3\theta}(a, b, c, \theta) = \int_0^\infty d\eta \eta \left[g(ab\eta, \theta, \lambda/2, c) - g(ab\eta, \theta, 0, c) \right]. \quad (63)$$

For the initial radius R_0 , we may again use $|X_0| + S_0$. If $g(s/S_0)$ is given by Eqs. (20), (31), and (56), we find that the form factor is

$$f_{3\theta} = -\sqrt{\pi} \frac{hS_0}{R_0^2} \cos \theta \exp \left[- \left[\frac{h \sin \theta}{S_0} \right]^2 \right]. \quad (64)$$

Equation (64) shows that $|\bar{\kappa}_{3\theta}|$ is maximum on the x -axis ($\theta = 0, \pi$). This is analogous to the situation for f_{3z} , which is determined primarily by $z = 0, \lambda/2$. Notice also that the maximum values of $|f_{3z}|$ and $|f_{3\theta}|$ agree at $z = 0, \lambda/2$ and $\theta = 0, \pi$, respectively, as they should because vorticity is divergence free.

D. Nonuniform Deposition of Energy

In asymmetry classes two and three (sections IV.B and C), we assumed that the pulse was distorted smoothly, similar to changes in shape of a deformable solid. Vorticity generation also takes place

when energy deposition is nonuniform within the envelope of a pulse. The simplest model of this situation would be that of N simultaneous small pulses within the envelope of the actual pulse and with the same integrated (total) energy as the actual pulse. To estimate the amount of vorticity generated in this model, we may extrapolate the results of Section IV.A for a pulse which is misaligned relative to a preformed, hot channel. Each of the N pulses will produce a hot channel through which the expanding shock waves produced by the other $N - 1$ pulses will pass. Taken separately, each pair of pulses, labeled by k and l , would produce two pairs of vortex filaments; Eq. (29) gives the approximate strength of each filament $\bar{\kappa}^{kl}$. Given that N is a small number and the pulses are sufficiently close, we remember from Section IV.A that the strength $\bar{\kappa}^{kl}$ will vary slowly with the displacement of pulses k and l . Thus we have $|\bar{\kappa}^{kl}| \approx \bar{\kappa}$ (constant). Since there are $N(N - 1)/2$ pairs of pulses, we find that convective mixing of characteristic strength $N(N - 1) \bar{\kappa}$ occurs when a small number N of simultaneous pulses are deposited close together. When the displacements of the pulses are greater than the radius of the channel which one of the pulses would produce separately (i.e., $X_0^{kl} > R_{1k} \approx R_{1l}$), the form factor in Eq. (29) decreases rapidly with increasing X_0^{kl} . Thus for a large number of pulses or for pulses which do not overlap, only "nearest neighbors" will interact to produce significant vorticity. The number N^* of nearest neighbors for each pulse will depend on geometry, and the resultant mixing strength will be proportional to $N N^* \bar{\kappa}$. We expect that the pulse sizes will determine the minimum scale of the turbulent structure observed in the composite channel produced by the collection of pulses. We will present further discussion of this higher order application of the theory and a comparison with relevant experimental data in a future article.

V. DETAILED NUMERICAL SIMULATIONS

We have performed preliminary detailed numerical simulations of this problem using the FAST2D⁹⁻¹¹ computer code in order to validate and calibrate the approximate analytic model developed above. The FAST2D code solves the two-dimensional equations for conservation of mass, momentum, and energy, employing the techniques of flux-corrected transport (FCT) and time step splitting. In addition to accounting for shocks properly, which the theoretical model does not do, the simulations are capable of describing the late-time motions and profiles as modified by the induced vorticity. Thus the various elements of the mixing-time approximations, and their significance, can be evaluated using detailed calculations of representative problems. In this section we will discuss simulations of examples of the two-dimensional asymmetry classes (1 and 2). The case of off center pulse propagation will receive more attention, since the vorticity strength will usually be greater than for smooth two-dimensional distortions and because the general features of the two cases are the same. We have addressed the question of channel cooling elsewhere^{5,6} in the context of convective cooling of lightning channels, and we will discuss complex multipulse turbulent flows in a future paper.

A. Off Center Pulse Propagation

Our simulations of off center pulse propagation utilize Cartesian coordinates and the configuration of Fig. 8, which shows a stationary, rectangular grid. Only the upper half plane appears in the calculation, since the x -axis forms a symmetry axis. The lower boundary is reflecting while the others are open. The grid consists of 100 by 30 cells of dimension δx and δy , each varying from 1 mm to 5 mm. To resolve the channel dynamics sufficiently, we have embedded a finely zoned region of 50×20 cells, each 1 mm on a side, in the center of the grid, where the axis of an initial 1.0 cm radius hot channel was positioned. With increasing distance from the central fine grid, the values of δx and δy transitioned smoothly from 1 mm to 5 mm. Near the sides and top of the grid, δx and δy were both 5 mm.

Figure 9 shows a plot of $\rho(x, 0, 0)$ and $P(x, 0, 0)$ (along the $y = 0$ plane) at the time the second pulse is deposited. Bennett profiles, $1/(1 + s^2 S_0^2)^2$, for the density and pressure deviation from ambient were used in these calculations. The dots (\bullet) on the two curves show the location and spacing (1 mm) of the finite difference grid points in the vicinity of the channel center.

To compute the vortex filament strength approximately we integrate the vorticity over the upper half plane to obtain

$$\bar{\kappa}_{1z}(t) = \int_{-\infty}^{\infty} dx \int_0^{\infty} dy \xi_z(x, y, t) = \int_{-\infty}^{\infty} dx v_x(x, 0, t) \approx \int_{x_{\min}}^{x_{\max}} dx v_x(x, 0, t) \quad (65)$$

where x_{\min} and x_{\max} are the respective limits of the coordinates on our grid. To derive Eq. (65) we have assumed that $v_x, v_y \rightarrow 0$ as $x, y \rightarrow \infty$.

Figure 10 shows the results of our calculations of $\bar{\kappa}_{1z}(t)$ for $\rho_{\infty}/\rho_0 = 10$, $R_0 = 0.4$, $R_1 = 1.3$ cm, $S_0 = 1.0$, and $X_0 = 1.0$ cm using the density profile of the channel formed by the first pulse and the pressure profile of the second pulse as shown in Fig. 9. Throughout the simulations, $\gamma \equiv c_p/c_v = 1.35$, where c_p and c_v are the specific heats for air with constant pressure and constant volume, respectively. After an initial positive transient and a weak relaxation oscillation, the integrated vorticity settles down to a steady state (negative) value. We may compare our formula, Eq. (29), for the vortex filament strength with the residual value shown in Fig. 10. If we assume $R_m \approx 1.0$ cm, $a \approx 0.4$, $b \approx 1.0$, and $c = 1.0$, then $f_{1z}(0.4, 1.0, 1.0) \approx -0.23$ from Fig. 15. Substituting these numbers into Eq. (29) with $U_m \approx c_s$ taken as 4×10^4 cm/sec gives $\bar{\kappa}_{1z}(\tau) \approx -1.9 \times 10^4$ cm²/sec. This number is within 10% of the value of -2.1×10^4 cm²/sec which we obtain from our simulations. The speed of sound c_s should be evaluated using only the density and temperature profiles of the preformed channel at the location of the center of the second pulse, i.e., $x = -X_0 = -1$ cm for the example here. The characteristic time τ must be approximately equal to $(R_1 - R_0)/(c_s/2) \approx 45 \mu s$ to justify using c_s as the

effective maximum expansion velocity of the heated cylinder. This value is within 25% of the observed value of $\tau \leq 60 \mu\text{s}$.

Using Eq. (6) with $x = 0$ and our theoretical value for $\bar{\kappa}_{1z}$ gives the maximum flow velocity expected in the symmetry plane.

$$v_{jet} = -1/2 v_{x,max} \approx \frac{\bar{\kappa}_{1z}}{\pi \bar{y}} \approx -76 \text{ m/s} \quad (66)$$

when $\bar{y} = 0.8 \text{ cm}$ (from the simulation). This value is in good agreement with the jet velocity of -85 m/s measured in the detailed simulations. The mixing time calculated from Eq. (10) using parameter values from the simulation is about $360 \mu\text{s}$.

In deriving Eq. (25) from Eq. (22) the time derivative term $\frac{\partial v}{\partial t}$, which must integrate to zero during the expansion, is neglected in favor of the $v \frac{\partial v}{\partial r}$ term, which is always of the same sign and hence contributes most to the integral over the interval $(0, \tau)$. A posteriori justification for this approximation is obtained from Fig. 10, which shows both the general cancellation of a big transient component, as assumed in Section IV, and good quantitative agreement with the residual vorticity term. This means that the amount of vorticity generated depends strongly on the eventual radial displacement of each fluid element but not on the detailed expansion history. The scale of the vorticity is set by an average expansion velocity only.

Figure 11 shows a schematic diagram to explain physically how the initial positive vorticity spike of Fig. 10 occurs. The expanding shock, shown at four different times as a dashed line, travels faster and drives the post shock flow faster in the low density material. We represent the density gradient as being localized between the two solid semi-circles in an annulus centered at S_0 . The shear resulting from the differential acceleration of the inner and the outer fluid corresponds to vorticity of positive sign which vanishes, as assumed, when differential velocity ceases. The angle between $\nabla \rho$ and ∇P (assumed normal to the dashed line shock fronts) appears at three locations along the original channel periphery. The residual vorticity, which corresponds to that appearing in Eqs. (25) and (28), in effect measures the net outward expansion of the new channel.

Figures 12 and 13 show the vorticity strength $\bar{\kappa}_{1z}(t)$ for several values of X_0 with the other remaining variables in our standard case held constant. When the axis of the second pulse fell within S_0 of the center of the channel (Fig. 12), the transient term appeared to oscillate more rapidly than the cases for which the axis of the second pulse fell "outside" the original channel (Fig. 13). The residual values $\bar{\kappa}_{1z}$ were also more nearly equal for the cases in Fig. 12 than for those in Fig. 13. The general

trend of $\bar{\kappa}_{12}(t \rightarrow \infty)$ in the five cases of Figs. 12 and 13 follows qualitatively the shape of $f_{12}(a, b, c)$ plotted for various cases in Figs. 5, 6, and 7. The uncanceled vorticity, which we called $\bar{\kappa}_{12}$ in Section III, decreases from a maximum around $X_0 = S_0$ both as $X_0 \rightarrow 0$ and as X_0 becomes large compared to S_0 . The ratio of $\bar{\kappa}_{12}$ at $X_0 = 0.2$ cm to $\bar{\kappa}_{12}$ at $X_0 = 0.1$ cm is probably not as small as expected from the curves f_{12} in Fig. 6 because the sound speed is higher when the second pulse is nearer the center of the preformed channel. The increasing sound speed partially counterbalances the tendency of f_{12} to fall off as X_0 approaches zero.

The major issue in interpreting these calculations using the formulae of Section III revolves around the choice of $U_m^2 \tau / 2$ for Eq. (28). For estimates in the case of off center pulse propagation, we have assumed U_m is the sound speed of the fluid at the center of the second pulse just before the second pulse is actually deposited. We have also assumed that the average expansion velocity is $U_m/2$.

Figure 14 compares the effects of initial pulse size on the second pulse, given constant values of the channel parameters and the overpressure and displacement, X_0 , of the second pulse. We notice that the transient term appears to scale in magnitude as R_0 while the value of the "residual" vorticity appears to scale as R_0^2 . We may explain the scaling of the residual vorticity in terms of our analytic "late time" treatment. Instead of using the estimate

$$U_m \approx c_s \quad (67)$$

we may calculate U_m from the equation

$$U_m \approx \frac{2(R_1 - R_0)}{\tau} \quad (68)$$

where τ is the time of expansion from R_0 to R_1 . In Fig. 14, we see that the extrema in $\bar{\kappa}_{12}$ for the cases of $R_0 = 0.2$ cm and 0.4 cm occur at almost the same values of t and that the relaxation to the final value of $\bar{\kappa}_{12}$ occurs at the same rate for the two cases. Thus we have (for any consistent definition of τ) the relation

$$\tau_A \approx \tau_B. \quad (69)$$

However we expect that

$$R_{1A} \approx \frac{1}{2} R_{1B} \quad (70)$$

since

$$R_{0A} = \frac{1}{2} R_{0B}. \quad (71)$$

Thus Eq. (68) yields

$$U_{mA} \approx \frac{1}{2} U_{mB}. \quad (72)$$

Estimates of the form factor indicate that

$$f_{1z}^A \approx f_{1z}^B. \quad (73)$$

Using Eqs. (31) and (46)-(51), we find that

$$\frac{\bar{\kappa}_{1z}^A}{\bar{\kappa}_{1z}^B} \approx \frac{(R_{1A} - R_{0A})^2}{(R_{1B} - R_{0B})^2} \approx \frac{1}{4} \quad (74)$$

for the case shown in Fig. 14.

This analysis indicates that c_s provides only a crude estimate of U_m as the energy deposited becomes small. From Eq. (69) and the fact that only the preformed channel was identical in cases A and B, we conclude that the relaxation time of the transients depends as much on the already existing density gradients as it does on the expansion of the new channel. The ambient sound speed at $X_0 = 1.0$ cm is about 4×10^4 cm/sec for the standard case and the reduced energy case of Fig. 14. The final relaxation to the long-time value $\bar{\kappa}_{1z}$ begins at about $40 \mu s$ for both cases, about the time required for a sound wave to reach the far side of the original hot channel from the edge of the second pulse (a distance of 1.8 cm and 1.6 cm for cases A and B respectively).

In Table I and Fig. 15, we present estimates of the form factor f_{1z} for the case $S_0 = 1.0$ cm, $R_0 = 0.4$ cm, $R_1 = 1.4$ cm, $\rho_\infty/\rho_0 = 10$ (channel formed by first pulse) and $P_0/P_\infty \approx 31$ (second pulse), as shown in Figs. 8 and 9. These values correspond to $a \approx 0.4$ and $b \approx 1.0$. We vary c from 0.2 to 2.0. To estimate the value of U_m , we used Eqs. (67) and (68). For Eq. (68), we define τ to be the time elapsed between the deposition of the second pulse ($t = 0$ in Figs. 13 and 14) and the last extremum in $\bar{\kappa}_{1z}$ before the monotonic relaxation to the residual value. The solid curve is the estimate from Eq. (30) using a Bennett density profile, Eq. (32), for the original channel. Near $c = 1.0$, Eq. (67) appears to provide a better estimate of U_m than does Eq. (68), at least when $R_0 = 1.0$ cm. Better agreement between the values of f_{1z} derived from simulations and the theory is expected when the energy deposition is slow and the adiabatic expansion treatment is a better approximation.

Finally, to illustrate the details of the flow resulting from off center pulse propagation, we have performed a simulation of two sequential, noncollinear pulses without the use of a symmetry plane. The Cartesian grid consists of 100×100 cells with 50×50 uniform fine cells in the center. The dimensions of the remaining cells increase geometrically to move the boundaries far away from the hot

channel. The first pulse deposits energy in the center at time $t = 0.0$ while the second occurs 1 ms later and deposits energy to the right of center ($X_0 = -0.5$ cm). The peak overpressures ($P_{\max} - P_{\infty}$) at the instants when energy deposition occurs are 4.7 atm and 2.4 atm, respectively. Again the pulses have Bennett profiles, Eq. (32), with a Bennett radius $S_0 = 0.5$ cm; thus we have $c = 1.0$. Figure 16 shows density contours and velocity vectors at $t = 1.26$ ms and density contours at $t = 2$ ms for the finely gridded central region. The noncollinearity of the pulses has produced an elongated, hot central core. In addition, the vector velocity plot clearly shows the enhanced flow between the two vortex filaments, which are separated by $2\bar{v} \approx 1.1$ cm or approximately 2 Bennett radii. This flow pulls the original hot channel (produced by the first pulse) toward the center of the second pulse, as predicted by our analytic theory. The diagram corresponding to $t = 2$ ms shows that the center of the original channel has cooled (has a higher density) as a result of this displacement. We observed identical phenomena in all similar simulations.

B. Two-Dimensional Distortions

To simulate vorticity generation by smooth two-dimensional distortions, we chose the case of an elliptical pulse as defined in Fig. 17. The parameters in Fig. 17 are typical of elliptical laser pulses used in recent studies by Greig et al.¹² We note that the pulse is much weaker than those considered in Subsection IV.A, and thus expect the residual vorticity to be lower in value. We use a constant value of $\gamma = 1.4$ for the ratio of principal specific heats. The Cartesian grid is quite similar to that used in the previous case, although more cells (150×75) are used. The embedded fine grid consists of 100×50 cells, and outside that region the x and y dimensions of the cells increase geometrically. This moves the boundaries far from the region of interest, permitting the shock to propagate well away from the hot channel before reaching the boundary. After pressure equilibrium of the hot elliptical channel is reached, we numerically eliminate the radial flows associated with the shock and follow only the incompressible flows associated with our mechanism for channel cooling. This permits use of longer time steps (factor of ~ 100) and reduces the running time significantly.

Figure 18 shows a sequence of density contour diagrams for this calculation. Defining the time $t = 0$ to coincide with the instantaneous deposition of energy, we see the shock wave moving out of the fine grid and leaving a hot channel with an elliptical cross section at $t \approx 50 \mu\text{s}$. The channel remains approximately the same for $t \approx 1$ ms and begins to distort noticeably by $t \approx 2$ ms under the influence of the flow shown in Fig. 2. This flow pattern continues to pull the channel outward along the x -axis as the two vortex filament pairs apparently move apart. Because a relatively coarse grid is used, these calculations do not resolve smaller scale turbulent structure which has been observed experimentally.¹² In addition, perturbations introduced experimentally might alter the interactions among

vortex filaments and, therefore, the flow pattern shown in our calculations at late times. However, this simulation should provide a useful treatment of the larger scale flows which determine the rate at which the ambient atmosphere mixes with the hot channel gas as a result of smooth two-dimensional distortions of a pulse.

To obtain an estimate for the strength of each vortex filament, of which four are present, we integrate the vorticity over the upper right quadrant $\{x \in (0, \infty), y \in (0, \infty)\}$ to obtain

$$\begin{aligned}\bar{\kappa}_{22}(t) &= \int_0^\infty dx v_x(x, 0, t) - \int_0^\infty dy v_y(0, y, t) \\ &\approx \int_0^{x_{\max}} dx v_x(x, 0, t) - \int_0^{y_{\max}} dy v_y(0, y, t)\end{aligned}\quad (75)$$

where x_{\max} and y_{\max} are the positive limits of our grid. In deriving Eq. (75) we have again assumed that $v_x, v_y \rightarrow 0$ and $x, y \rightarrow \infty$. Figure 19 shows the evolution of $\bar{\kappa}_{22}$ for the elliptical channel simulation. As we have indicated in Fig. 2, the residual vorticity in the upper right hand quadrant should be positive, the flow being inward at the ends of the major axis and outward along the minor axis. During the expansion to pressure equilibrium, however, the acceleration term $\partial v / \partial t$ induces a transient negative vorticity. By our previous definition, τ_{\max} appears to be $\leq 75 \mu s$ and the residual vorticity is $\approx 2.7 \times 10^2 \text{ cm}^2/\text{s}$. Defining $R^2(t) = a(t) b(t)$ where $a(t)$ and $b(t)$ are the semimajor and semiminor axes of the ellipse, we have $R_0 \approx 0.25 \text{ cm}$. Adiabatic expansion would give us $R_1 \approx 0.36$ and $\rho_\infty / \rho_0 \approx 2$ for the hot channel at pressure equilibrium, and from the simulation, we obtain $U_m \leq 3 \times 10^3 \text{ cm/s}$, which is less than the ambient value of c_s by an order of magnitude. From Figs. 2 and 17, we find that $S_0 \approx 0.31$ and $X_0 \approx 0.19$. From Eq. (52) and the ensuing discussion, we obtain $|f_{22}| \approx 1$. We may now use Eq. (49) to find an estimate of $|\bar{\kappa}_{22}|$ (theory) $\leq 2.3 \times 10^2 \text{ cm}^2/\text{s}$. Theory and simulation, therefore, agree within a factor of 20%.

VI. CONCLUSIONS

This paper represents a first step in analyzing the cooling of hot channels produced by local energy deposition in a gaseous medium. We have identified a mechanism which produces sufficient rotational motion to account for the cooling rates of electric discharge channels produced in the laboratory.¹⁻⁵ As the channel expands to pressure equilibrium, a shock is produced, and asymmetries between pressure and density gradients generate vorticity according to Eq. (1). After pressure equilibration and propagation of the shock wave well away from the hot channel, vorticity is no longer generated; however, significant residual vorticity exists. We may represent the resulting flow field in terms of one or more vortex filament pairs of strength $\pm \bar{\kappa}_{i\alpha}$, where $i = 1, 2, 3$ labels the type of asymmetry and $\alpha = z$ or θ , labels the vector component of the vorticity. The strength $\bar{\kappa}_{i\alpha}$ satisfies the equation

$$\bar{\kappa}_{1a} = \frac{U_m^2 \tau}{2} \ln \left(\frac{\rho_\infty}{\rho_0} \right) f_{1a} \quad (76)$$

where U_m is the expansion velocity of the channel boundary when the expansion flux $U(t) R(t)$ is a maximum; ρ_∞ and ρ_0 are the ambient density and the density at the center of the hot channel just after energy deposition; and f_{1a} is a form factor which may be evaluated from the formulae presented in Section IV. For asymmetry class 1 (off center pulse propagation), $U_m \approx c_s$ since the flows at the channel boundary generate most of the vorticity. For smooth distortions of the pulse envelope, which belong to asymmetry classes 2 and 3, $U_m < c_s$, since the subsonic interior flows generate most of the residual vorticity. We have also identified another subclass of pulse distortions which arise from energy deposition (within the envelope of a pulse) which does not follow a smooth functional form such as the Bennett profile of Eq. (40). As a simple model we might consider deposition to occur as several simultaneous packets of energy within the boundary of the pulse. In a future paper we will analyze and simulate this situation in detail using the FAST2D code. Accurate numerical simulations of examples of the two-dimensional asymmetry classes have revealed good agreement with Eq. (76).

With an estimate for \bar{V} , which appears from simulations to be $\approx S_0$ and Eq. (76) for κ_{1a} , we may obtain values for the mixing time scales τ_{mix} from Eqs. (10a-e). For the two-dimensional asymmetry classes τ_{mix} is the approximate time for doubling of the volume. For three-dimensional distortions, $\bar{\kappa}_{3a}$ and $\bar{\kappa}_{3z}$ are both nonnegligible, and the cumulative effects of the two components must be calculated to obtain a reasonable doubling time for the channel volume. The values of $\tau_{\text{mix}(z)}$ and $\tau_{\text{mix}(\theta)}$ given by Eqs. (10a) and (10e) do, however, provide a useful estimate of the importance of each component relative to the other and to other types of asymmetry.

ACKNOWLEDGMENTS

The authors are most grateful to B. Greig, M. Raleigh, R. Fernsler, and M. Lampe for their careful investigation and testing of the theory and the resulting enhancement of our understanding of the related phenomena.

We also thank the Defense Advanced Research Projects Agency and the Office of Naval Research for providing the financial support for this work.

REFERENCES

1. J.R. Greig, R.E. Pechacek, R.F. Fernsler, I.M. Vitkovitsky, A.W. DeSilva, and D.W. Koopman, NRL Memo. Rep. 3647 (1977).

2. J.R. Greig, D.W. Koopman, R.F. Fernsler, R.E. Pechacek, I.M. Vitkovitsky, and A.W. Ali, Phys. Rev. Lett. **41**, 174-176 (1978).
3. D. Koopman, J. Greig, R. Pechacek, A. Ali, I. Vitkovitsky and R. Fernsler, J. Phys. (Paris), Colloque C7, Supp. au n°7, Tome 40, Juillet 1979, C7-419-420.
4. M. Raleigh, J.D. Sethian, L. Allen, J.R. Greig, R.B. Fiorito, and R.F. Fernsler, NRL Memo. Rep. 4220 (1980).
5. J.M. Picone, J.P. Boris, J.R. Greig, M. Raleigh, and R.F. Fernsler, J. Atmos. Sci., **38** (No. 9), 2056-62 (1981).
6. J.M. Picone, J.P. Boris, J.R. Greig, M. Raleigh, and R.F. Fernsler, NRL Memo. Rep. 4472, Appendix (1981).
7. S. Kainer and M. Lampe, NRL Memo. Rep. 4247 (1980).
8. H. Lamb, *Hydrodynamics*, 6th ed. (Dover, New York, 1945), Chapter I.
9. J.P. Boris, NRL Memo. Rep. 3237 (1976).
10. J.P. Boris, Comments on Plasma Physics and Controlled Fusion, **3** (No. 1), pp 1-13, (1977).
11. D.L. Book, J.P. Boris, A.L. Kuhl, E.S. Oran, J.M. Picone, and S.T. Zalesak in Proceedings of Seventh International Conference on Numerical Methods in Fluid Dynamics, edited by William C. Reynolds and Robert W. MacCormack (Stanford Univ.-NASA Ames, 1980), 1981, pp. 84-90.
12. J.R. Greig, R.E. Pechacek, M. Raleigh, and K.A. Gerber, NRL Memo. Rep. 4826 (1982).

Table I — Values of f_{12} from numerical simulations. The displacement of the axes of the hot channel and the latest pulse ($c \equiv v_y S_0$) varies from 0.2-2.0. The table also compares two methods of computing U_m . The sound speed c_s is computed at the position of the pulse just prior to energy deposition.

c	$U_m = C_s(X_0)$	$-f_{12}(C_s)$	U_m (eq.68)	$-f_{12}$ (eq.68)	$-\bar{\kappa}_{12}(\tau)$
0.2	$8.2 \times 10^4 \frac{\text{cm}}{\text{sec}}$	0.10	$8.0 \times 10^4 \frac{\text{cm}}{\text{sec}}$	0.10	$1.9 \times 10^4 \frac{\text{cm}^2}{\text{sec}}$
0.5	5.2×10^4	0.18	6.3×10^4	0.14	2.1×10^4
1.0	3.9×10^4	0.23	5.9×10^4	0.15	2.1×10^4
1.5	3.6×10^4	0.19	4.2×10^4	0.17	1.6×10^4
2.0	3.5×10^4	0.15	3.2×10^4	0.16	1.2×10^4

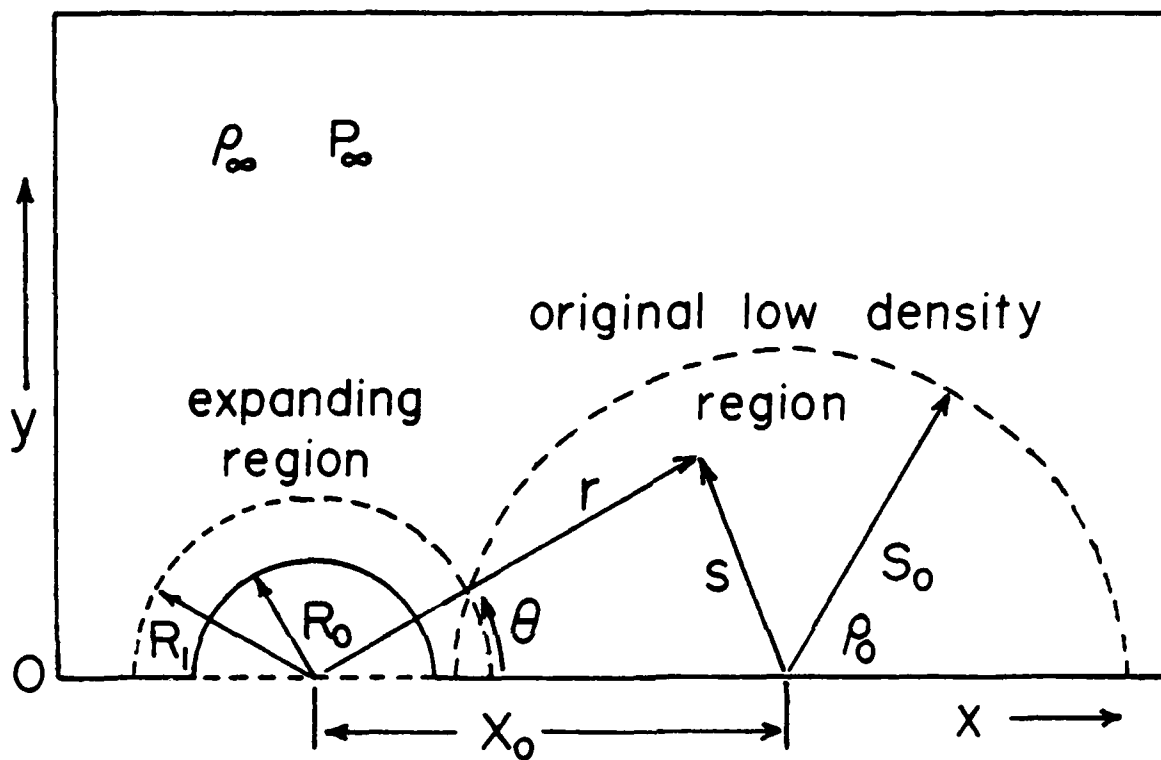


Fig. 1 — Schematic of asymmetry class one, in which a cylindrical pulse of radius R_0 propagates parallel to a hot channel of characteristic radius S_0 formed by a previous pulse. The second pulse, offset from the first pulse by X_0 , expands to radius R_1 .

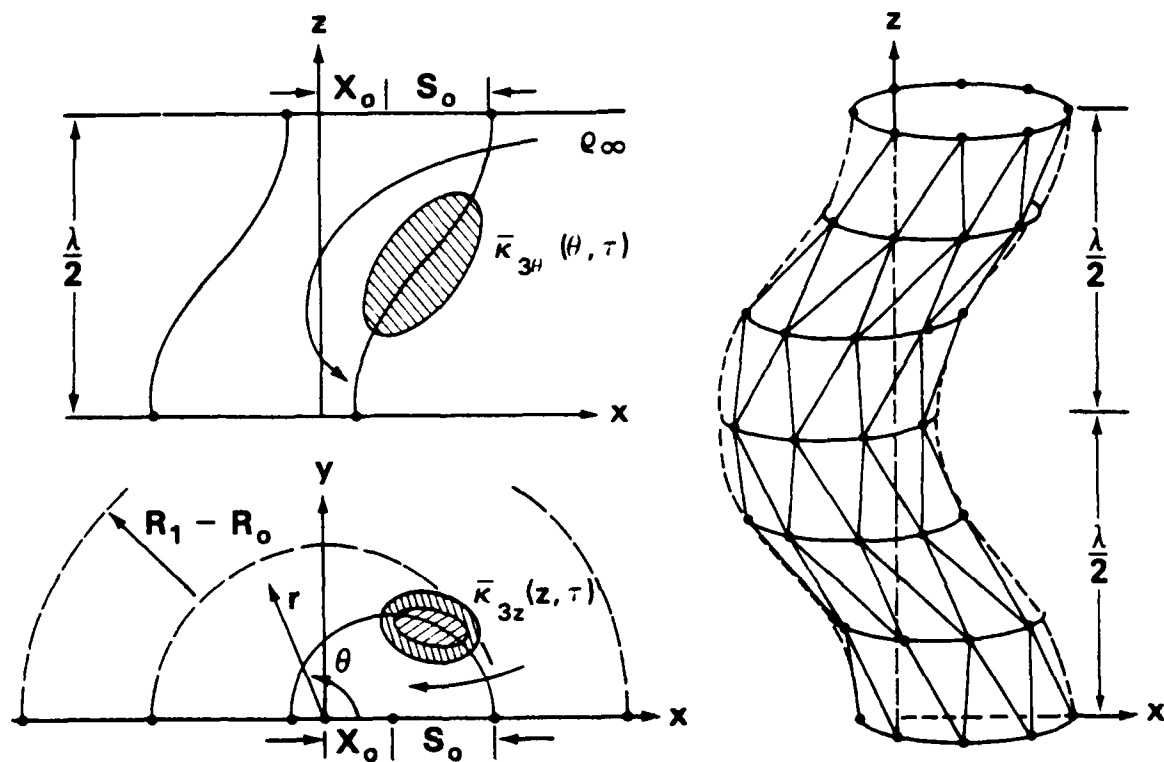
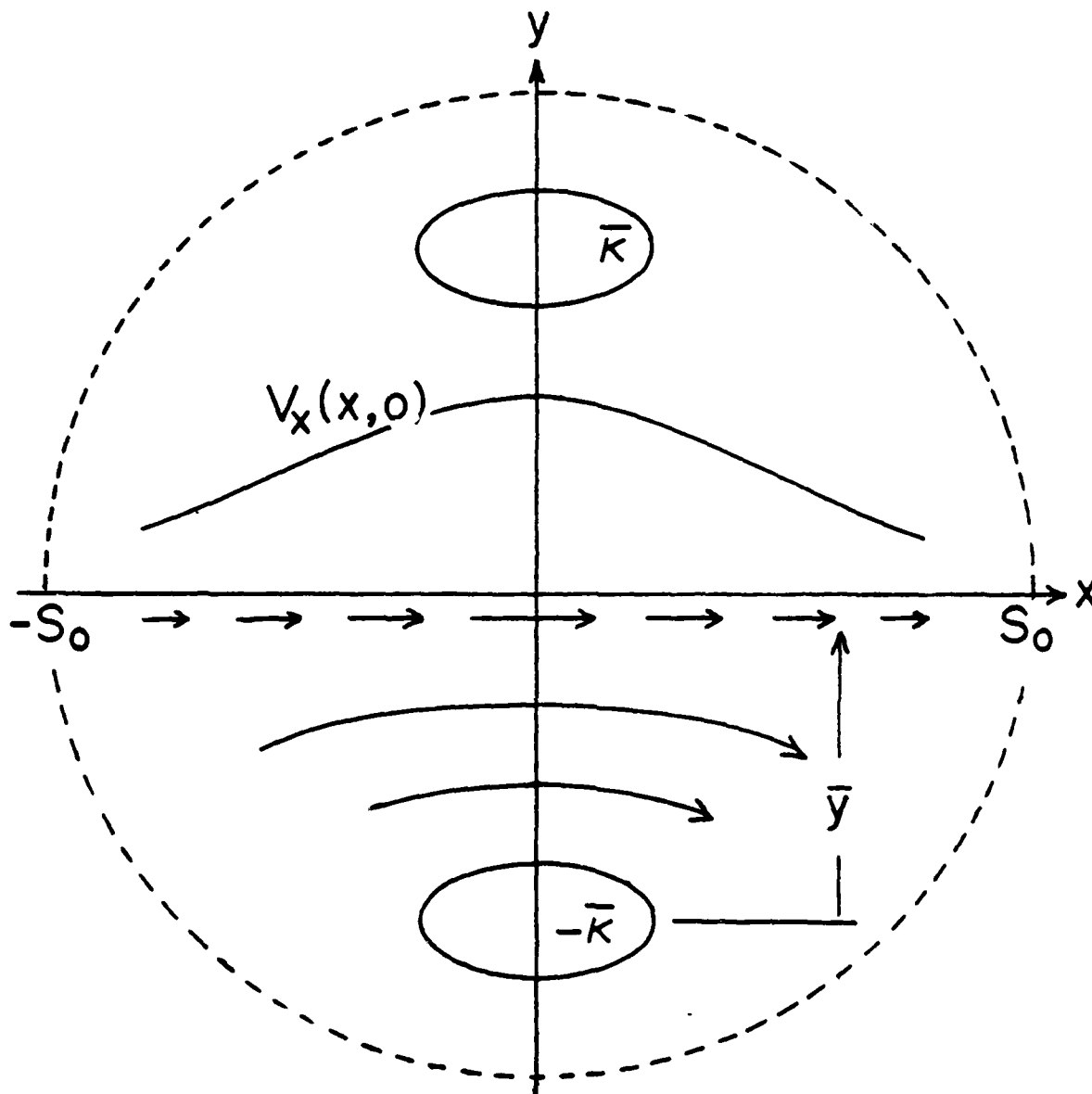


Fig. 3 — We model asymmetry class three by treating a sinusoidal channel section of wavelength λ . This will generate nonnegligible τ and θ components of the vorticity. The flow field approaches cylindrical symmetry about the center of mass (z -axis) while the density distribution is offset from the z -axis by X_0 , which varies with position along the z -axis.



$$\tau_{\text{mix}} = \frac{2\pi S_0}{|\bar{\kappa}| \bar{y}} \left[S_0^2/3 + \bar{y}^2 \right]$$

Fig. 4 — Symmetric distribution of localized vorticity appears as two extended vortex filaments of strength $\pm \bar{\kappa}$ and separation $2\bar{y}$. The flow velocity induced by these vortices is shown along the x-axis halfway between the filaments. If we have a hot channel of radius S_0 , about which the filaments are centered, we may define a mixing time scale as the time required for a fluid element at $x = -S_0$ to reach $x = S_0$. We exclude the effects of smaller scale turbulent motion which might exist at the boundaries or in the interior of the channel. (Here we acknowledge the existence of a similar figure, appearing in *Journal of the Atmospheric Sciences*.)

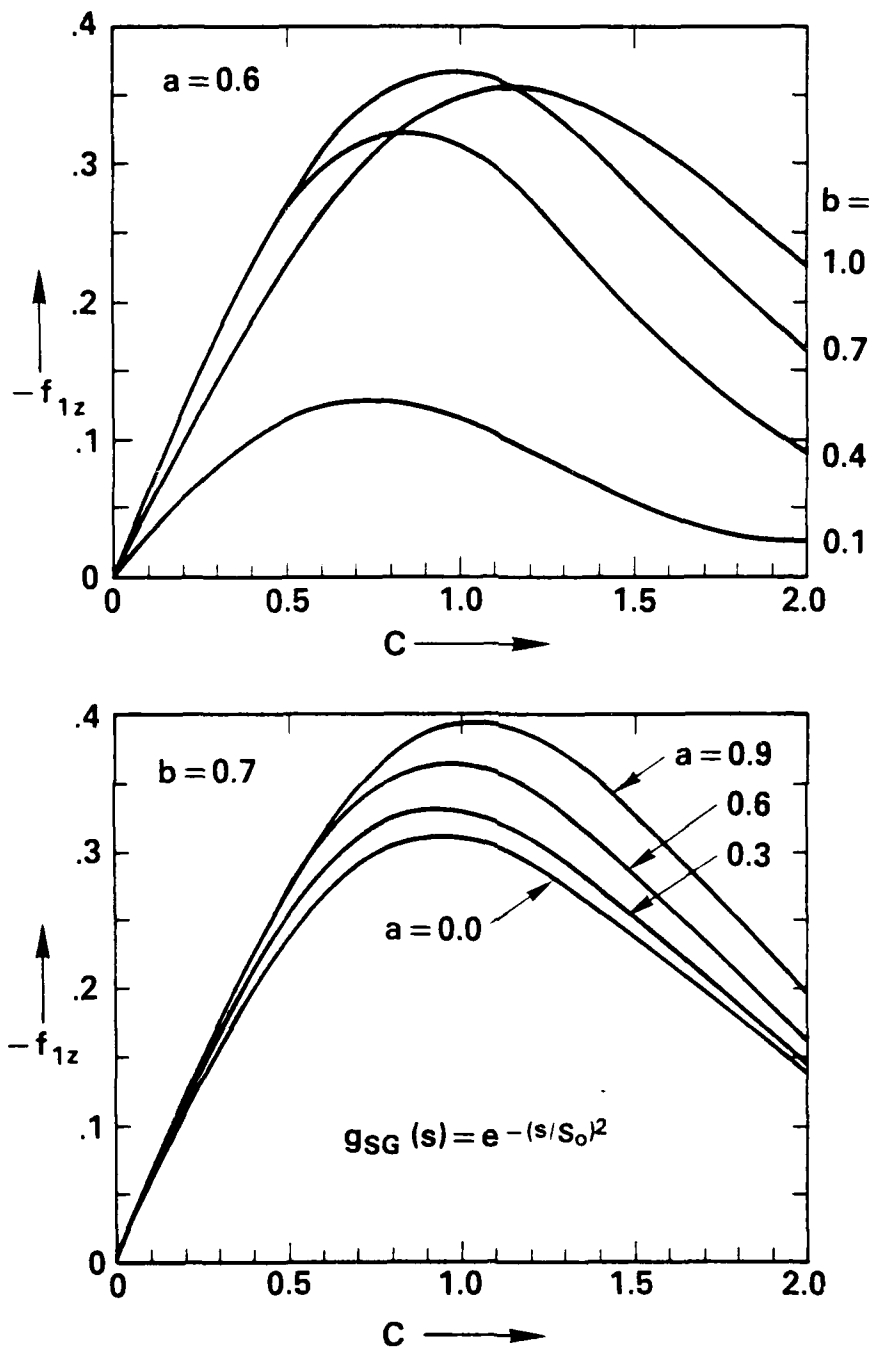


Fig. 5 — Integrated vorticity form factors assuming a "super-Gaussian" density profile. Larger variation occurs with b in the upper figure than with a in the lower figure. We find peak vorticity generation in the vicinity of $V_1 = S_1$ for all cases. The maximum magnitude of the form factor ranges from 0.1 to 0.4 with 0.3 being a representative value for quick estimates.

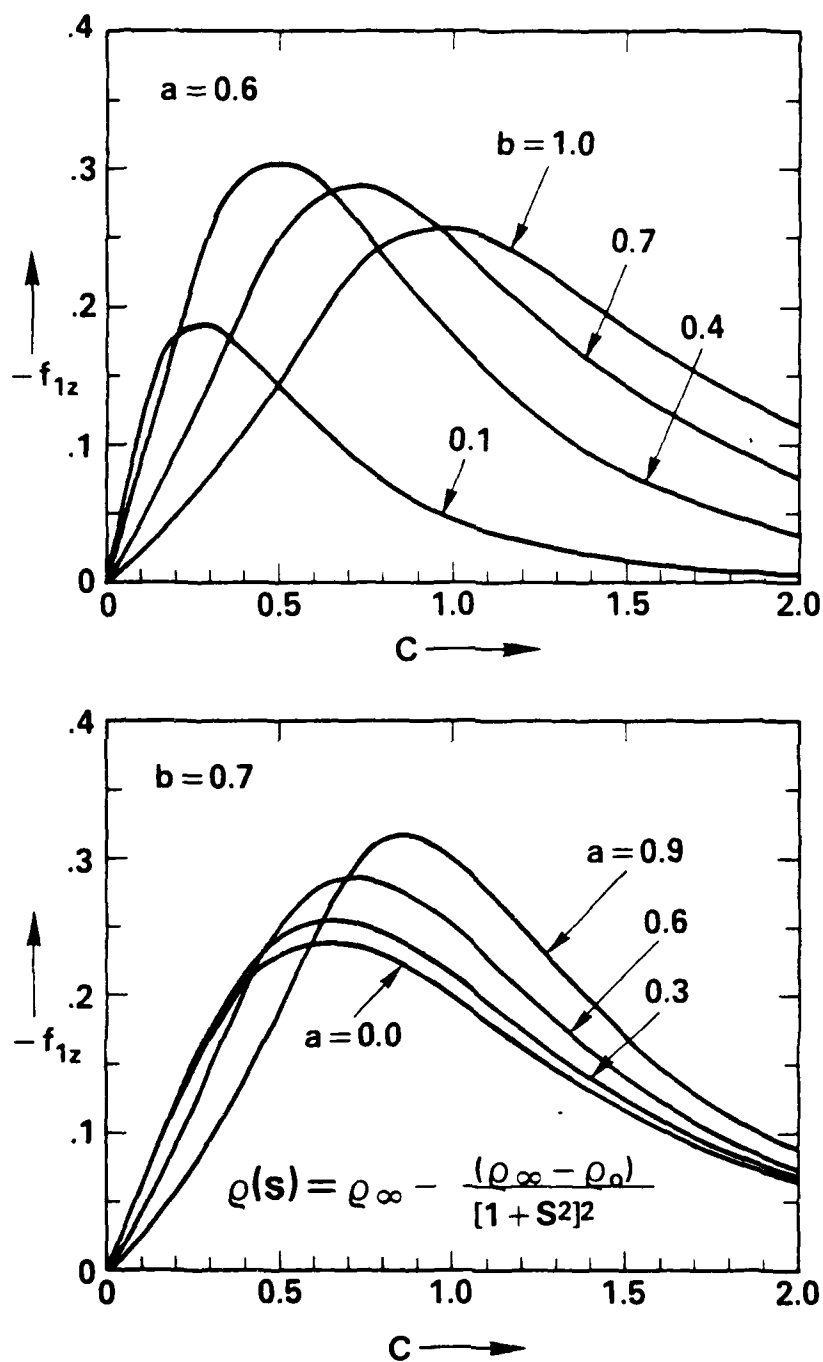


Fig. 6 — Integrated vorticity form factors assuming a Bennett density profile. Again the form factors vary more with b than with a . Note that appreciable form factors can exist at $V_0 \approx 0.2 S_0$ when b is small.

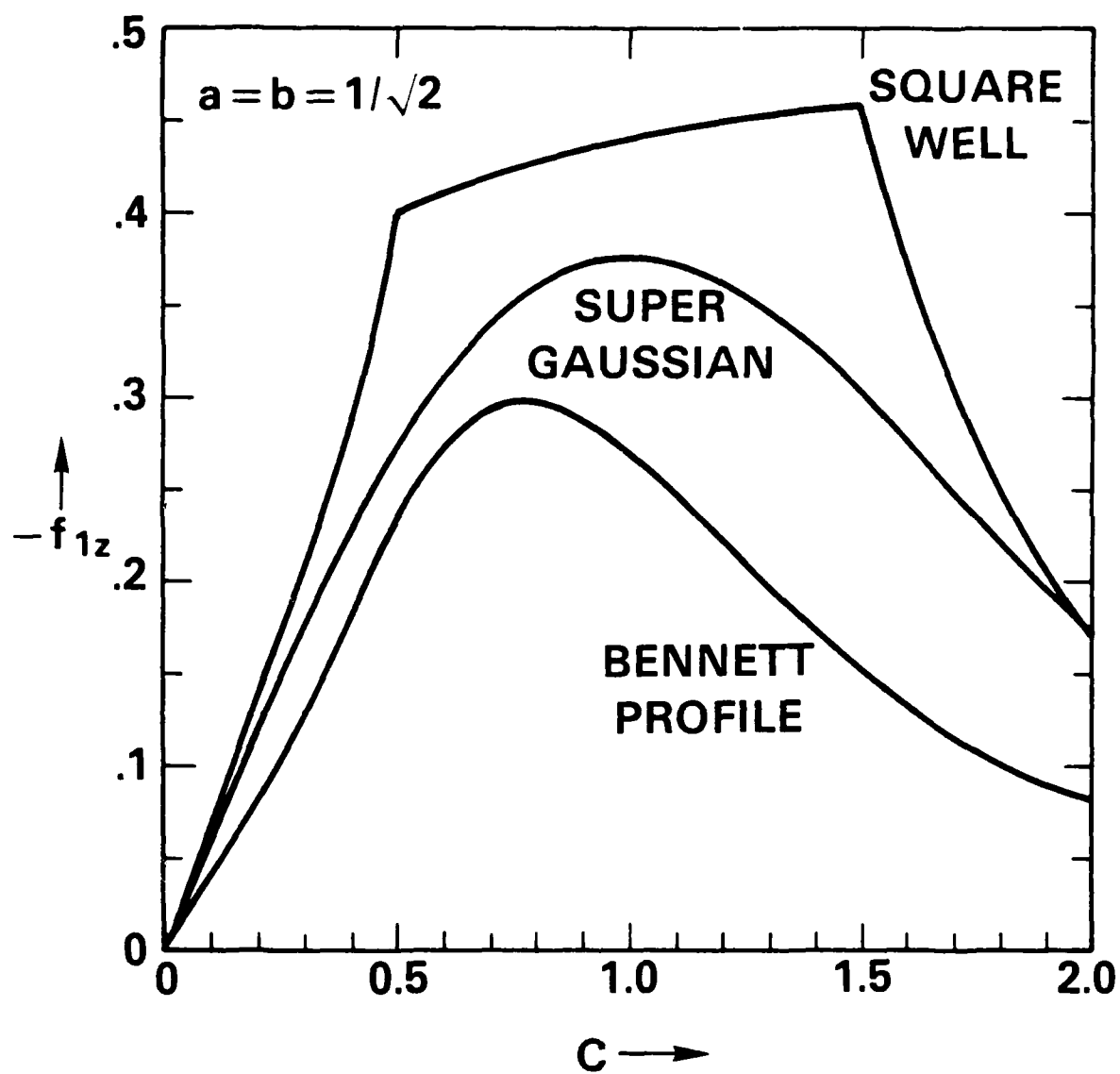


Fig. 7 — Comparison of integrated vorticity form factors for three distinct density profiles at $a = b = 1/\sqrt{2}$. The variation among form factors is relatively small for widely differing density profiles.

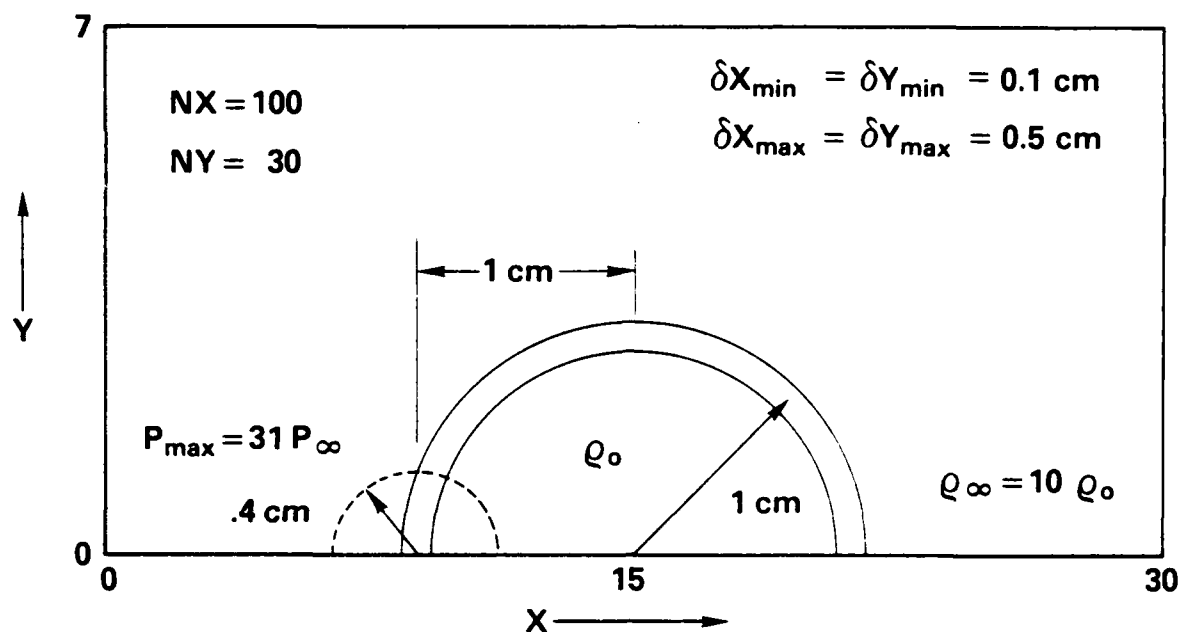


Fig. 8 — Initial conditions for numerical simulations of vorticity generation when a pulse propagates parallel to but offset from an existing hot channel. The simulations include only the upper half plane with a reflecting lower boundary and outflow conditions at the other boundaries. By stretching the outermost zones by a factor of five, we move the boundaries far from the active region.

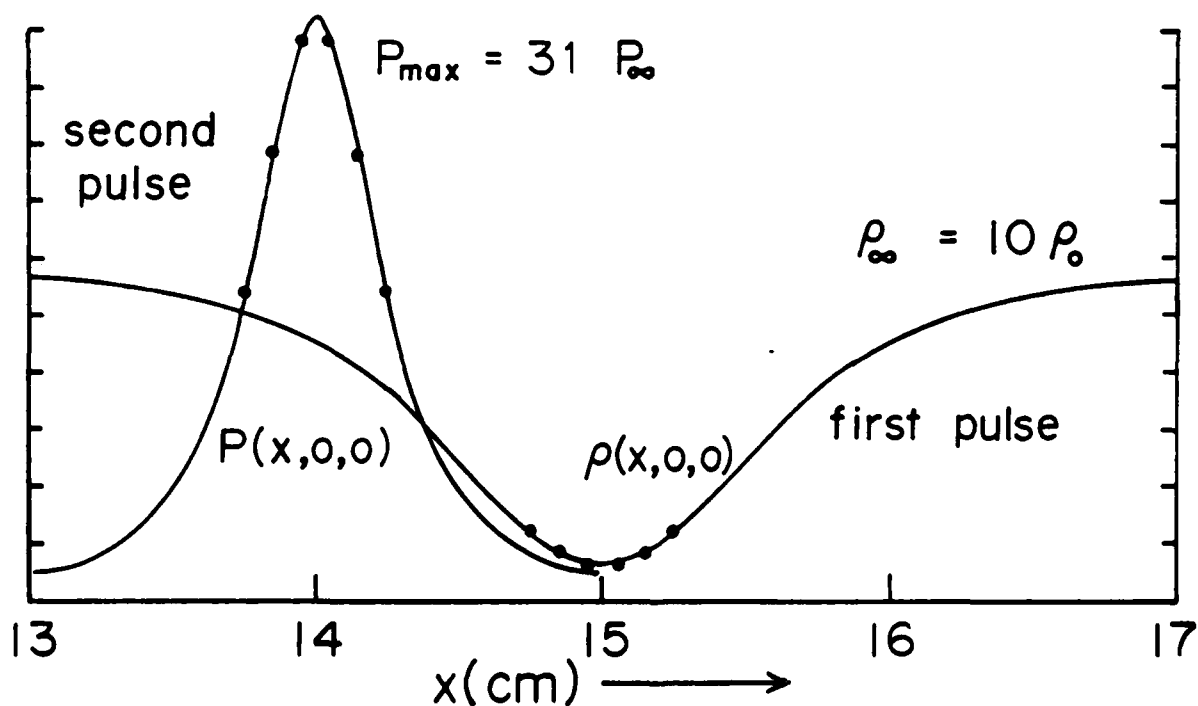


Fig. 9 — Pressure and density profiles along the symmetry ($x-z$) plane when the axes of the hot channel and the latest pulse are separated by 1.0 cm. The characteristic radius of the channel is 1.0 cm and that of the latest pulse is 0.4 cm (Figs. 1 and 8). The data points correspond to cell centers and indicate the resolution provided by the fine zones.

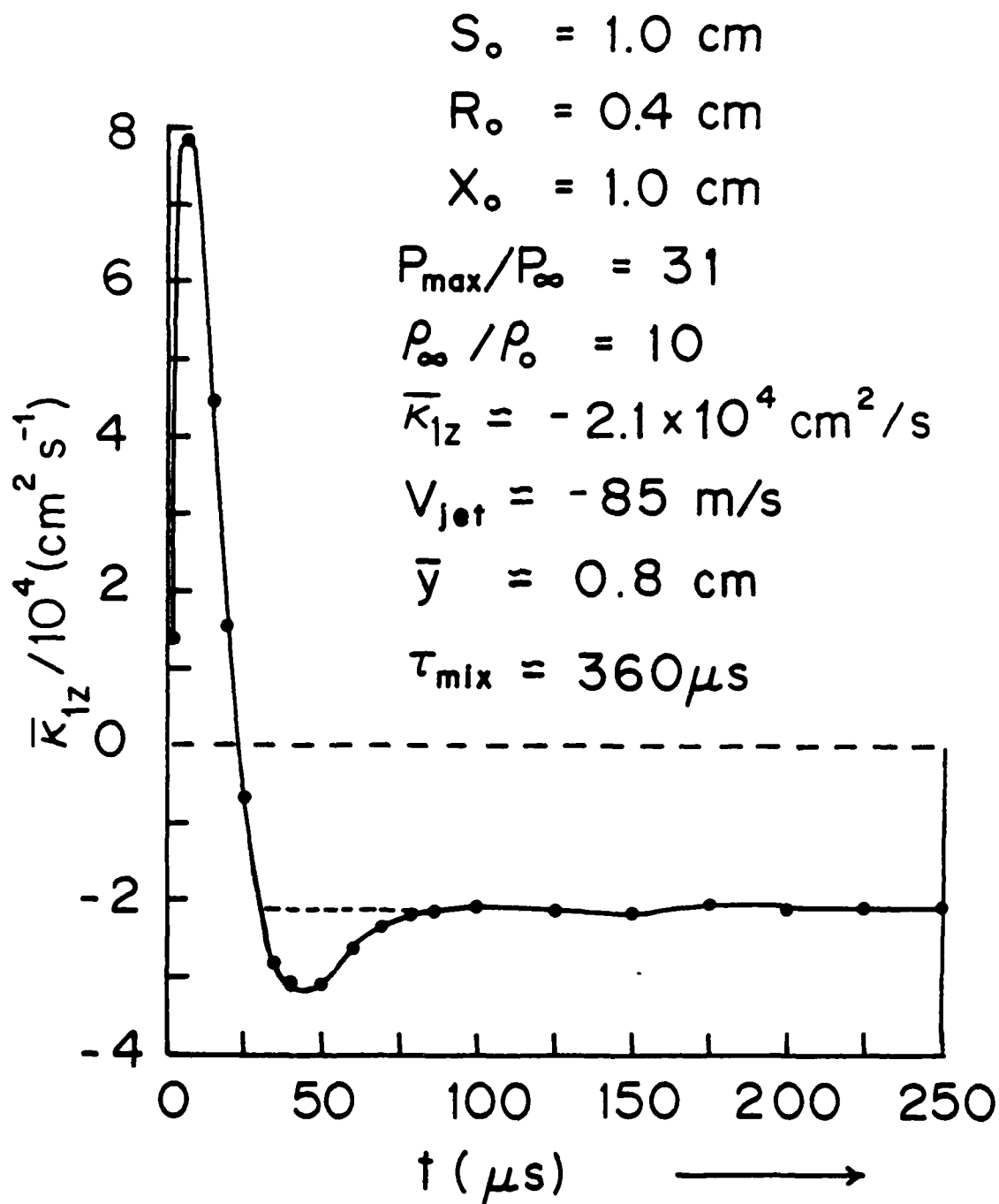


Fig. 10 — Time history of the vorticity strength in the upper half plane for our standard case. The integrated vorticity over the entire plane is zero, since an oppositely directed vortex filament having a strength of equal magnitude is generated in the lower half plane.

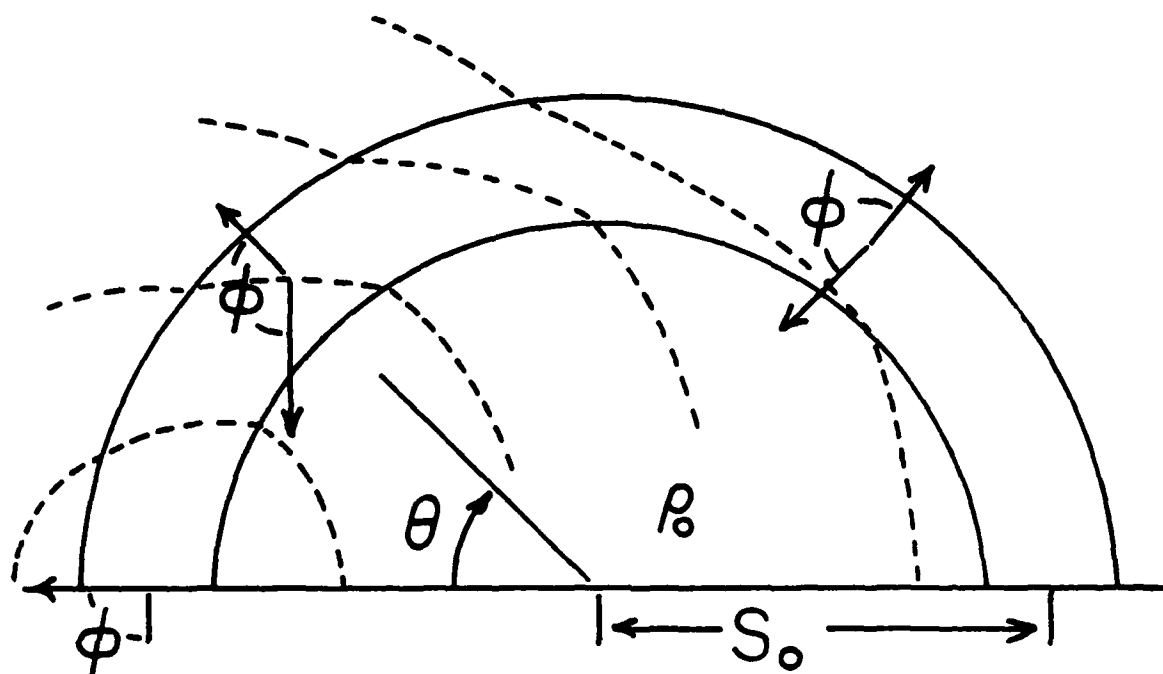


Fig. 11 — Schematic diagram showing how the initial vorticity transient arises physically for the situation in Fig. 1. The quantity ϕ is the angle between the pressure gradient of the expansion flow and the density gradient of the initial hot channel. When the outwardly expanding fluid eventually decelerates to rest, the acceleration (and therefore the pressure gradient) must change sign, causing most of the transient vorticity to cancel.

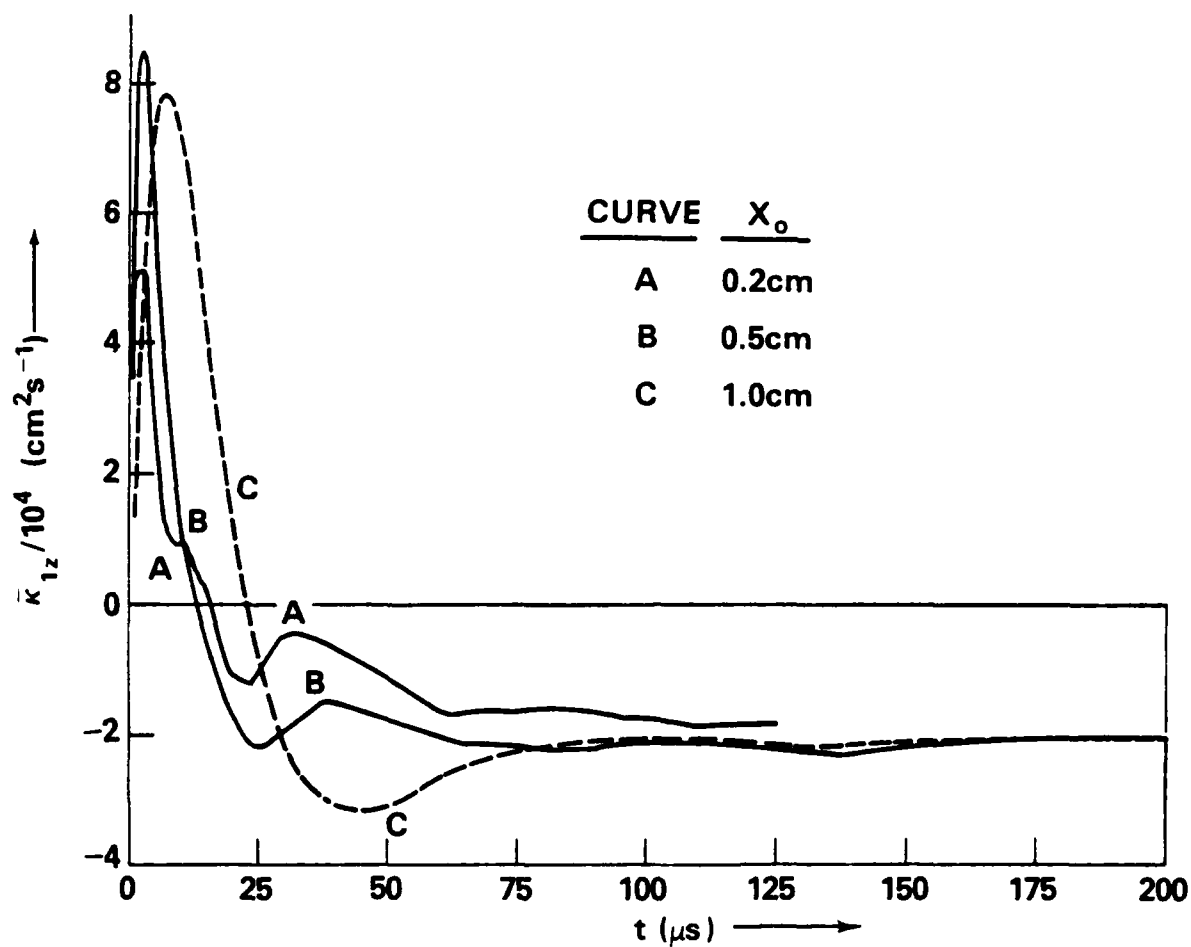


Fig. 12 — Integrated vorticity $\bar{\kappa}_{1z}(t)$ for three cases with $\Lambda_0 \leq S_0$.

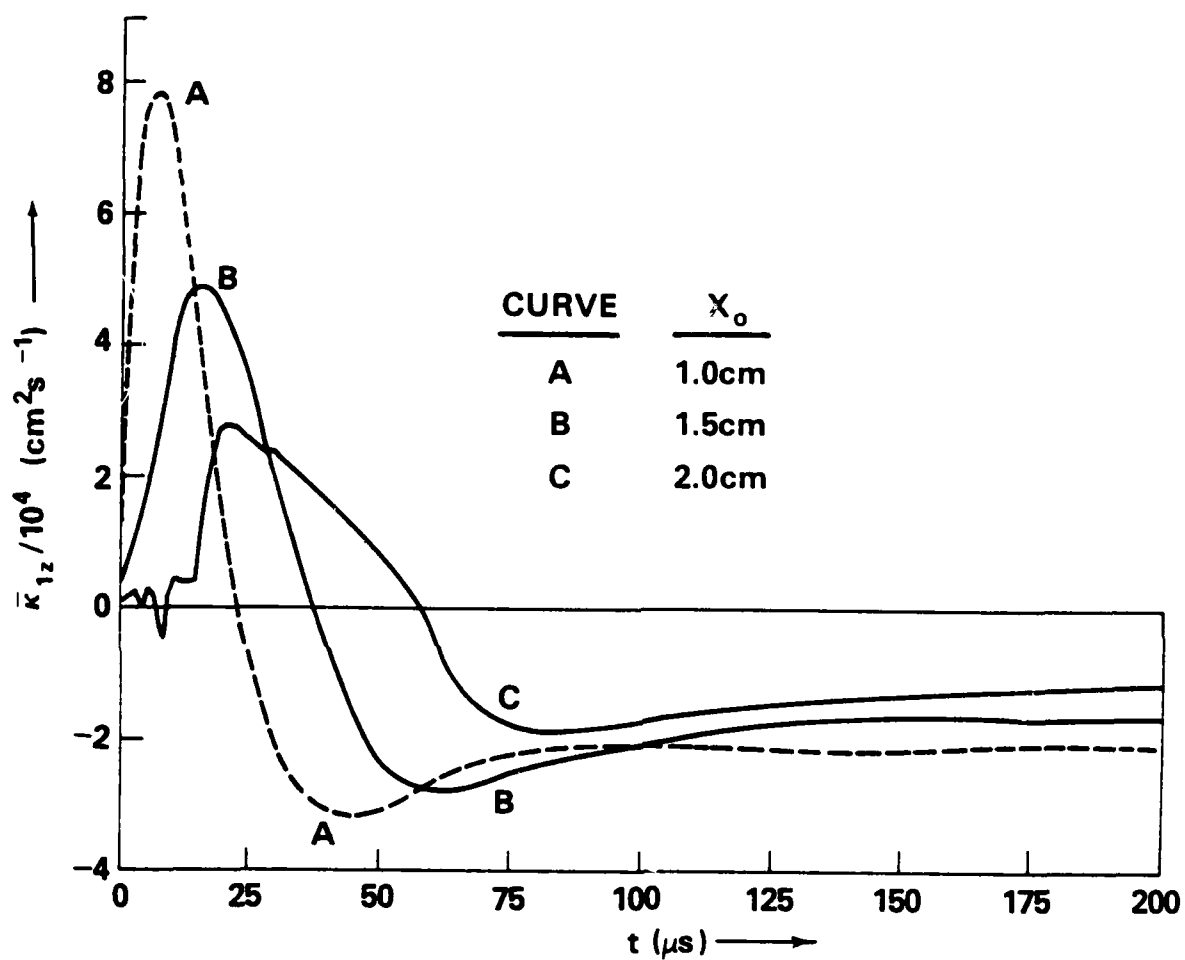


Fig. 13 — Integrated vorticity $\bar{\kappa}_{1z}(t)$ for three cases with $X_0 \geq S_0$.

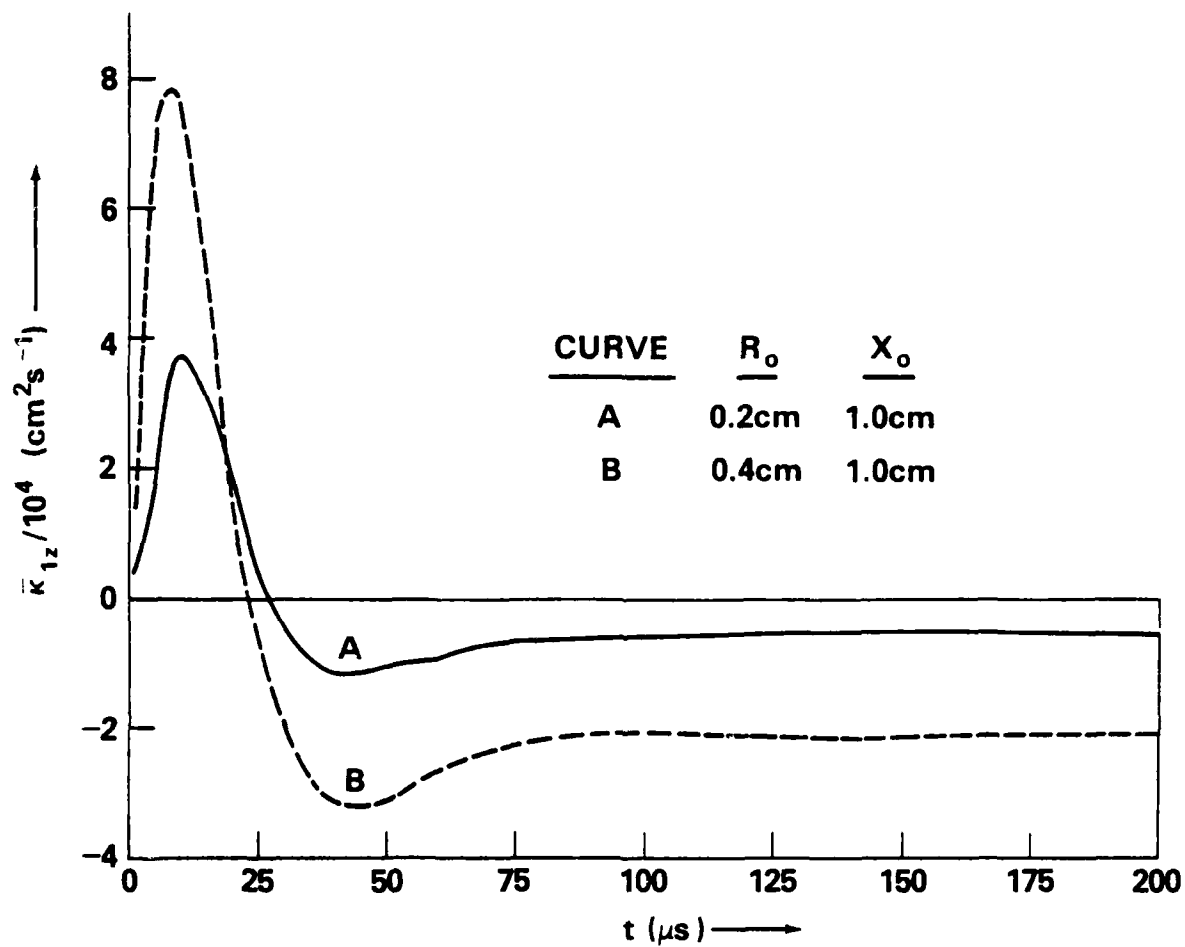


Fig. 14 — Integrated vorticity $\bar{\kappa}_{1z}$ for two cases differing only in the radius of the second pulse. Curve B is the standard case and curve A has one-fourth the energy per unit length in one-fourth the area, so that the peak overpressures are equal. The transients differ in amplitude by a factor of two but the residual integrated vorticity differs by a factor of four.

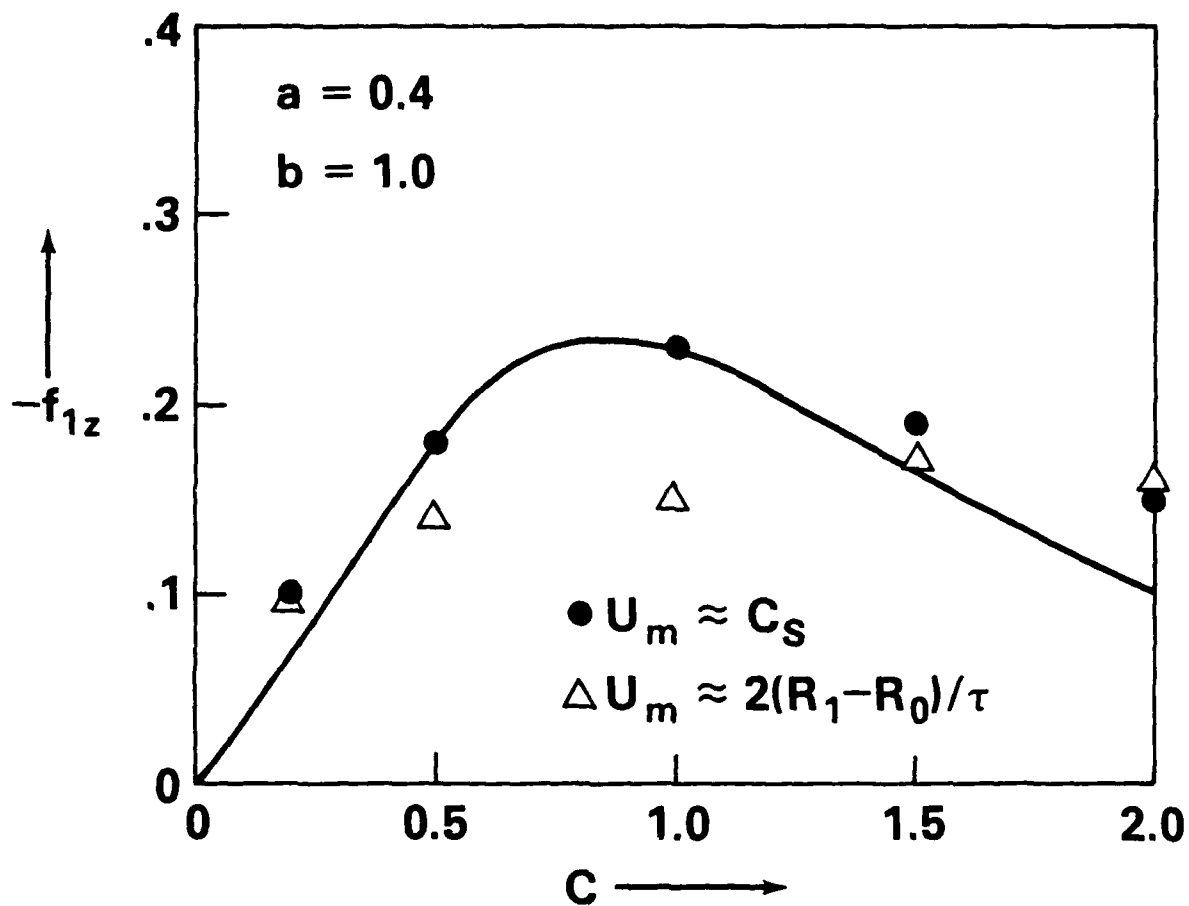


Fig. 15 — Comparison of numerically determined form factor (denoted by \bullet and \triangle) to the theoretical calculation based on Eq. (30) and $a = 0.4$ and $b = 1.0$. Agreement is good for both magnitude and sign.

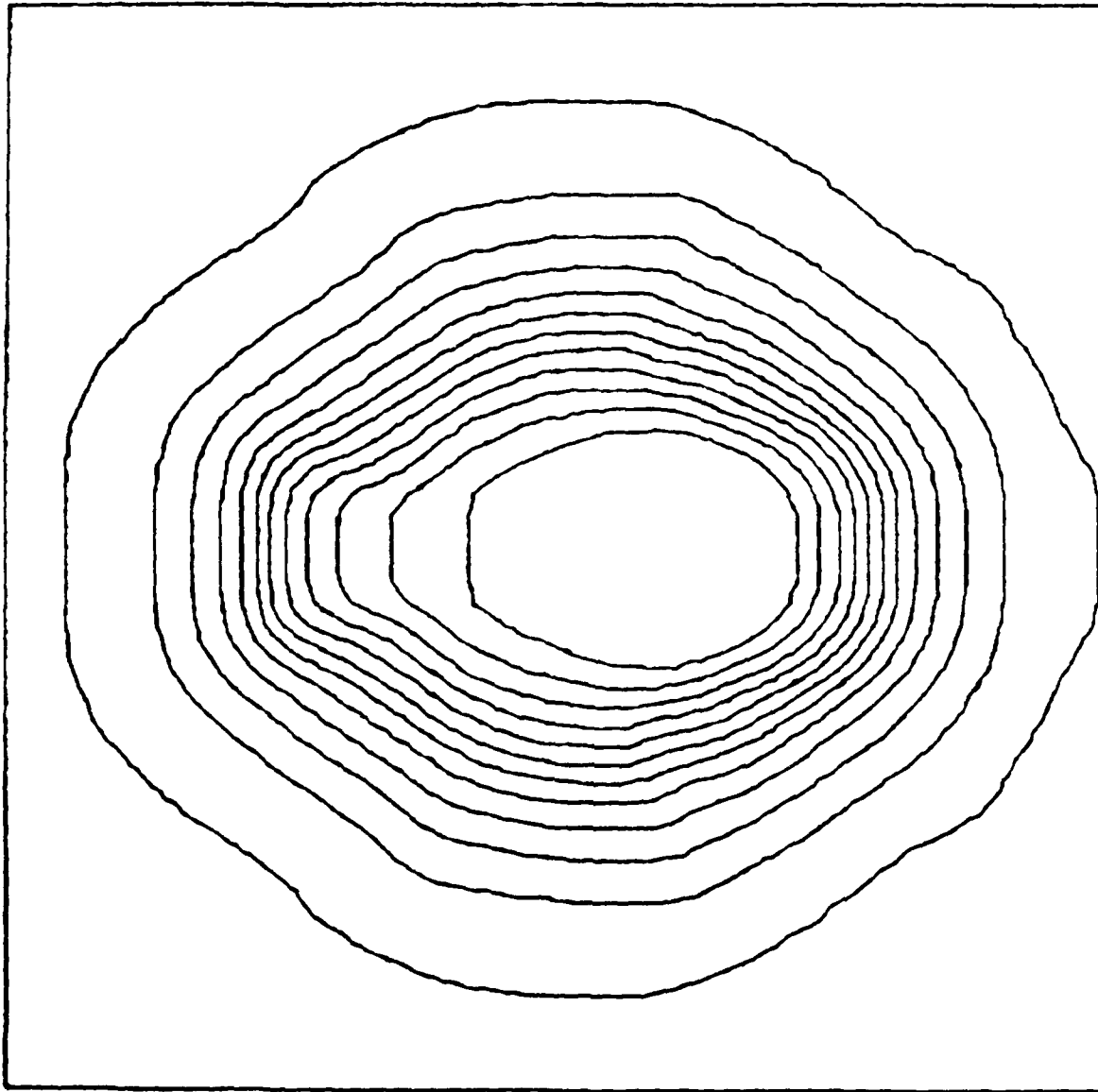


Fig. 16 — (a) Density contours and (b) velocity vectors at a time $t = 1.26$ ms and (c) density contours at $t = 2.00$ ms for two sequential noncollinear pulses. The first pulse occurred at $t = 0.0$ ms in the center of the grid, and the second pulse occurred at $t \approx 1.0$ ms with a displacement of 0.5 cm to the (reader's) right of center. The figures correspond to the fine grid. The density contours vary from 3.0×10^{-4} (innermost) to 1.1×10^{-3} gm/cm³ (outermost). In (b), we have plotted a velocity vector at every other cell center; thus the centers of the two vortex filaments are somewhat indistinct. The major flow occurs between the filaments and the direction of the flow is from the center of the earlier pulse to the center of the later pulse.

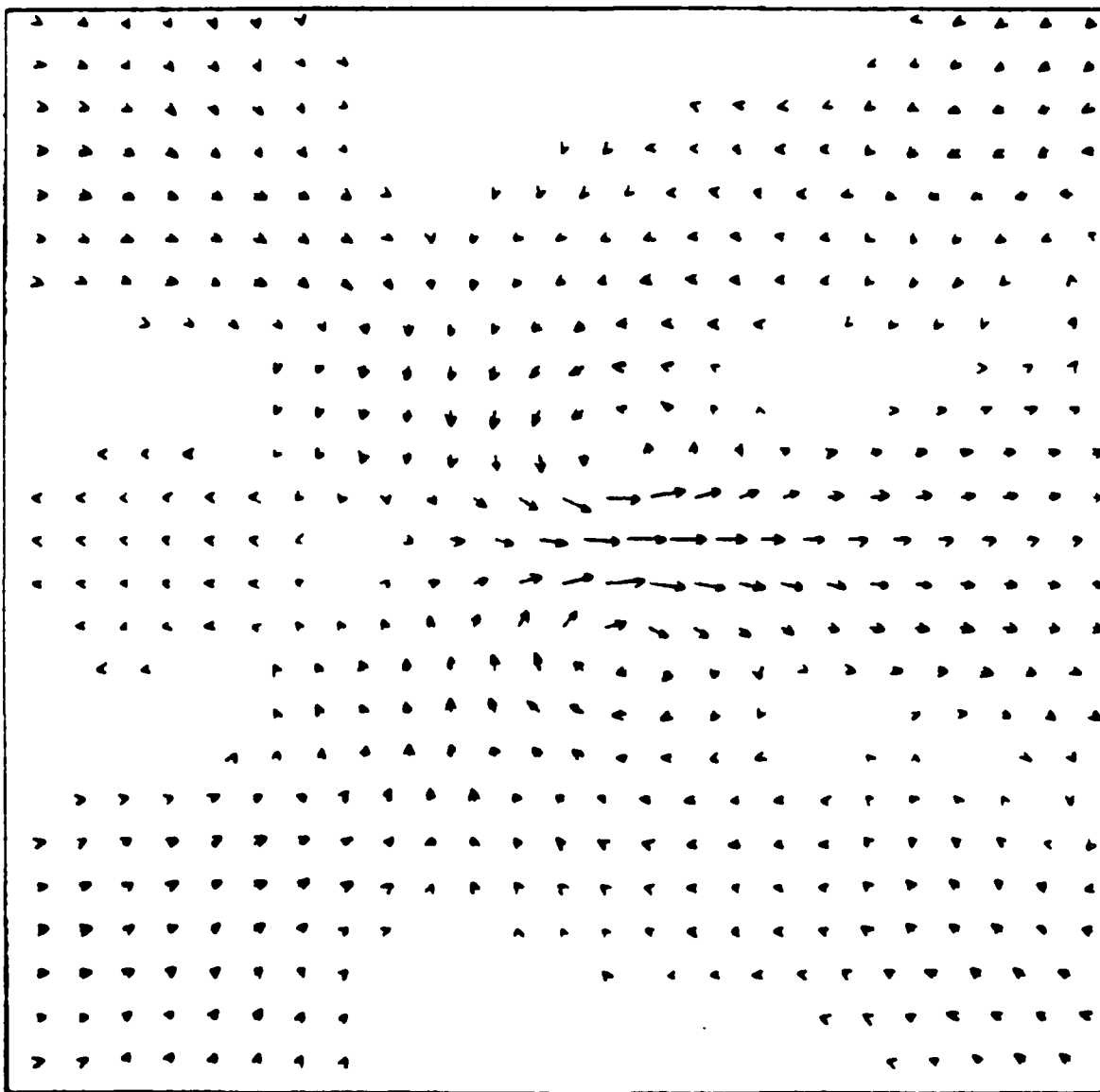


Fig. 16 — (a) Density contours and (b) velocity vectors at a time $t = 1.26$ ms and (c) density contours at $t = 2.00$ ms for two sequential noncollinear pulses. The first pulse occurred at $t = 0.0$ ms in the center of the grid, and the second pulse occurred at $t \approx 1.0$ ms with a displacement of 0.5 cm to the (reader's) right of center. The figures correspond to the fine grid. The density contours vary from 3.0×10^{-4} (innermost) to 1.1×10^{-3} gm/cm³ (outermost). In (b), we have plotted a velocity vector at every other cell center; thus the centers of the two vortex filaments are somewhat indistinct. The major flow occurs between the filaments and the direction of the flow is from the center of the earlier pulse to the center of the later pulse.

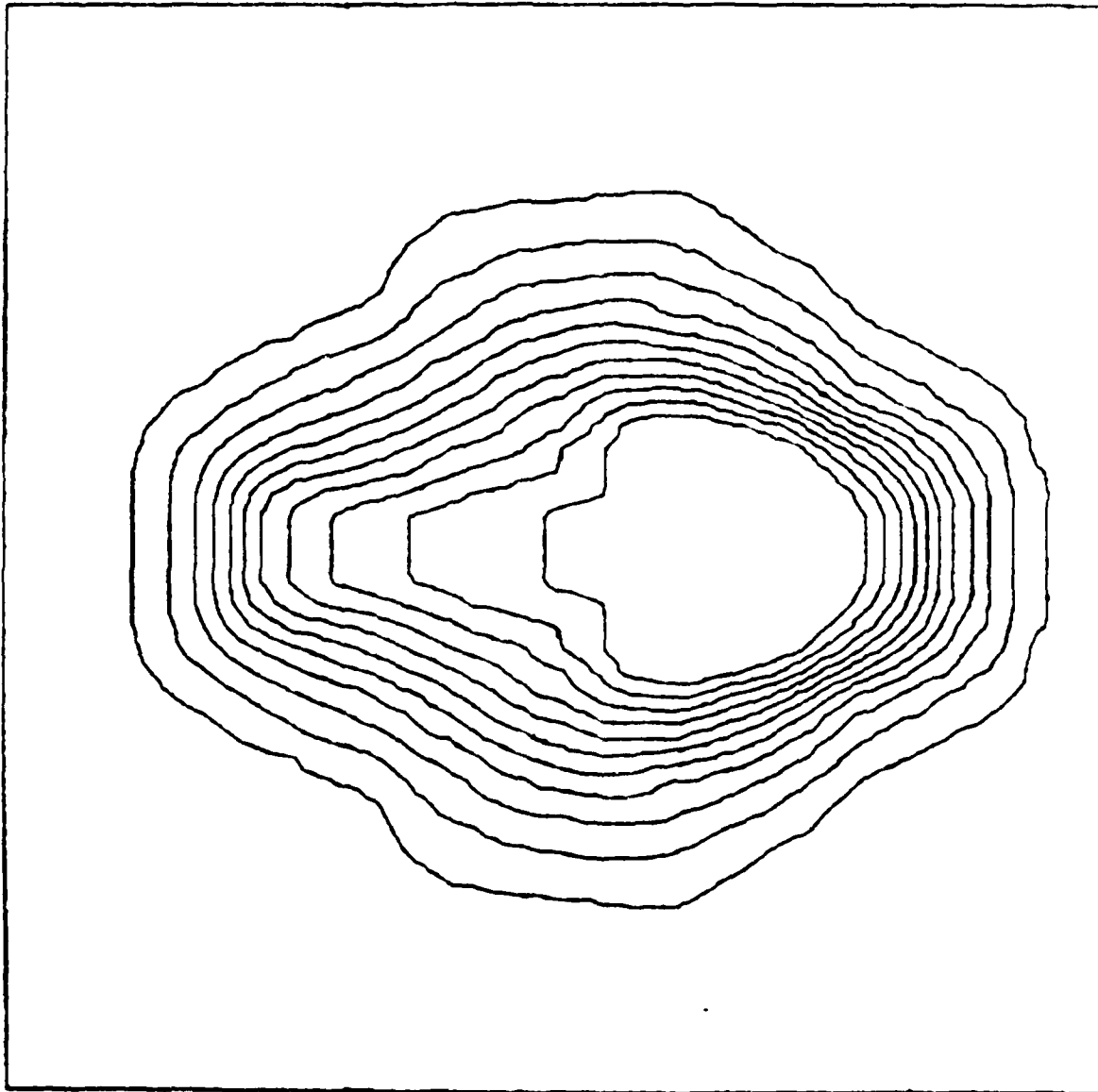


Fig. 16 — (a) Density contours and (b) velocity vectors at a time $t = 1.26$ ms and (c) density contours at $t = 2.00$ ms for two sequential noncollinear pulses. The first pulse occurred at $t = 0.0$ ms in the center of the grid, and the second pulse occurred at $t \approx 1.0$ ms with a displacement of 0.5 cm to the (reader's) right of center. The figures correspond to the fine grid. The density contours vary from 3.0×10^{-4} (innermost) to 1.1×10^{-3} gm/cm³ (outermost). In (b), we have plotted a velocity vector at every other cell center; thus the centers of the two vortex filaments are somewhat indistinct. The major flow occurs between the filaments and the direction of the flow is from the center of the earlier pulse to the center of the later pulse.

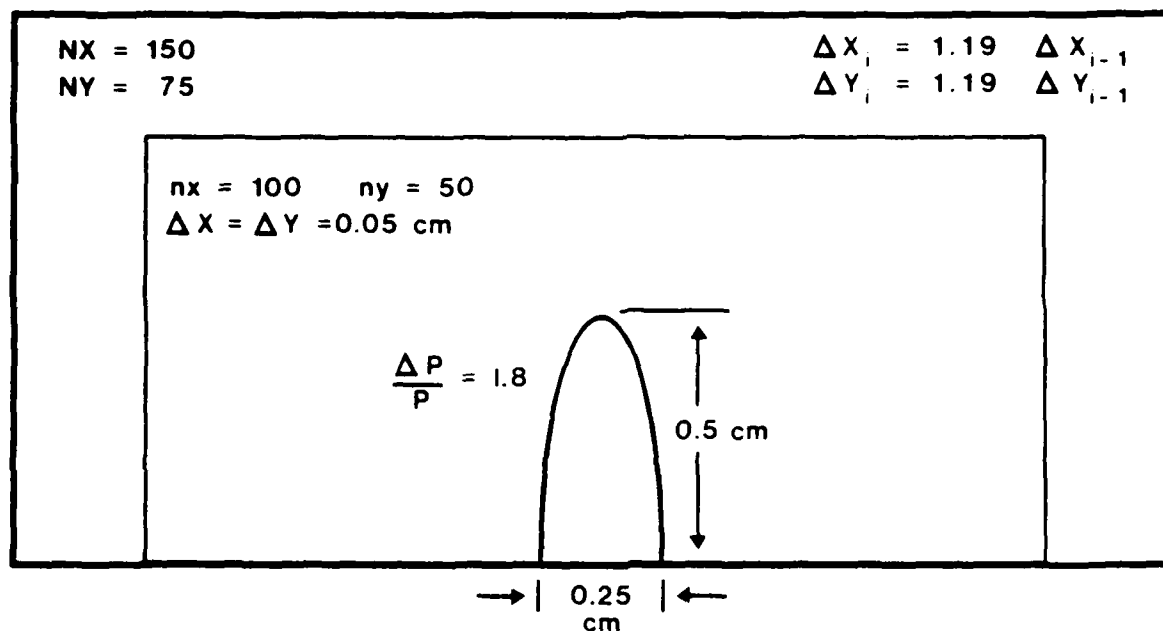


Fig. 17 — This schematic shows the initial conditions and Cartesian grid for our numerical simulation of vorticity generation by an elliptical pulse. We simulate only the portion of the pulse above the $x-z$ symmetry plane, surrounding the pulse with a uniform grid of 100×50 fine cells. The dimensions of the remaining cells then increase geometrically with distance from the pulse.

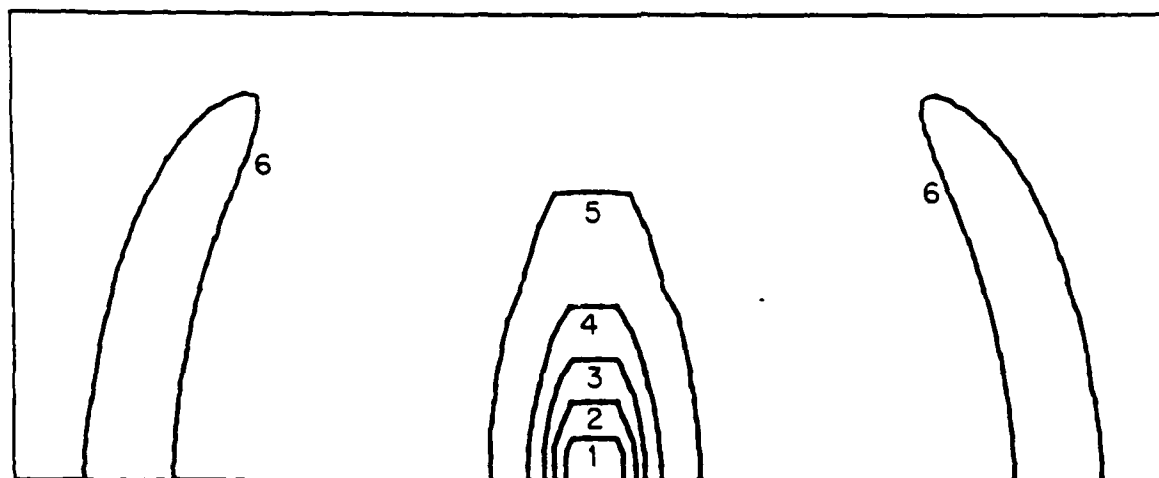


Fig. 18 — Results of a computer simulation of the time development of a laser pulse having smooth elliptical distortion. The simulation used the initial conditions described in Fig. 17. The density contour diagrams shown here correspond to the following time intervals elapsed from the point of instantaneous energy deposition: (a) $36 \mu s$, (b) $75 \mu s$, (c) 2.0 ms , (d) 4.0 ms , and (e) 6.4 ms . The six equally spaced contour values range from $7.4 \times 10^{-4} \text{ g/cm}^3$ (contour 1) to $1.26 \times 10^{-3} \text{ g/cm}^3$ (contour 6); the contour values increase with increasing vertical displacement from the center of the channel. In (a), the shock appears just inside the fine grid. Diagram (b) shows contours 1-5 and the others have only contours 2-5, indicating that the channel gas has cooled somewhat. The flattened tops of the contours result from clipping by the flux-corrected transport algorithm.

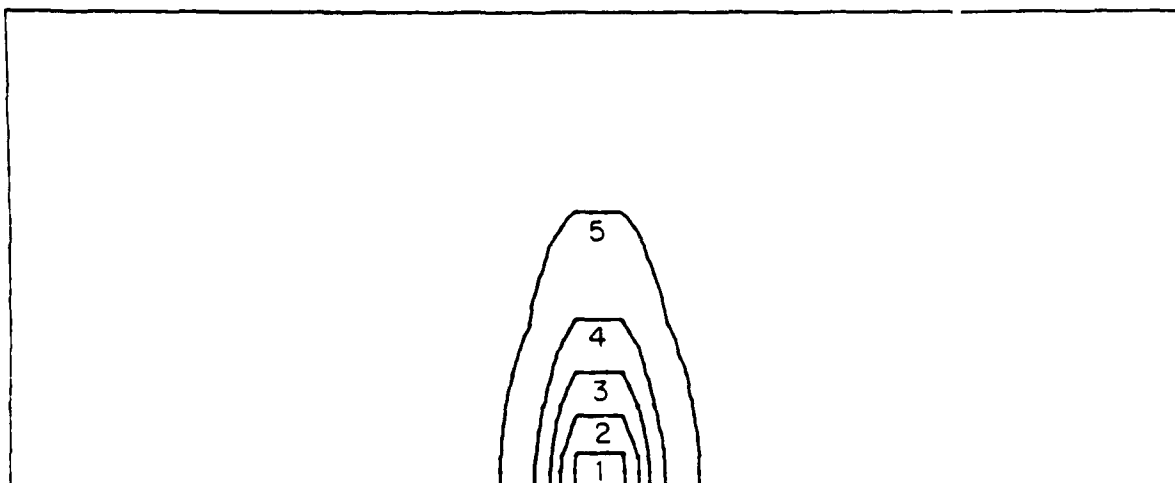


Fig. 18 — Results of a computer simulation of the time development of a laser pulse having smooth elliptical distortion. The simulation used the initial conditions described in Fig. 17. The density contour diagrams shown here correspond to the following time intervals elapsed from the point of instantaneous energy deposition: (a) $36 \mu\text{s}$, (b) $75 \mu\text{s}$, (c) 2.0 ms , (d) 4.0 ms , and (e) 6.4 ms . The six equally spaced contour values range from $7.4 \times 10^{-4} \text{ g/cm}^3$ (contour 1) to $1.26 \times 10^{-3} \text{ g/cm}^3$ (contour 6); the contour values increase with increasing vertical displacement from the center of the channel. In (a), the shock appears just inside the fine grid. Diagram (b) shows contours 1-5 and the others have only contours 2-5, indicating that the channel gas has cooled somewhat. The flattened tops of the contours result from clipping by the flux-corrected transport algorithm.

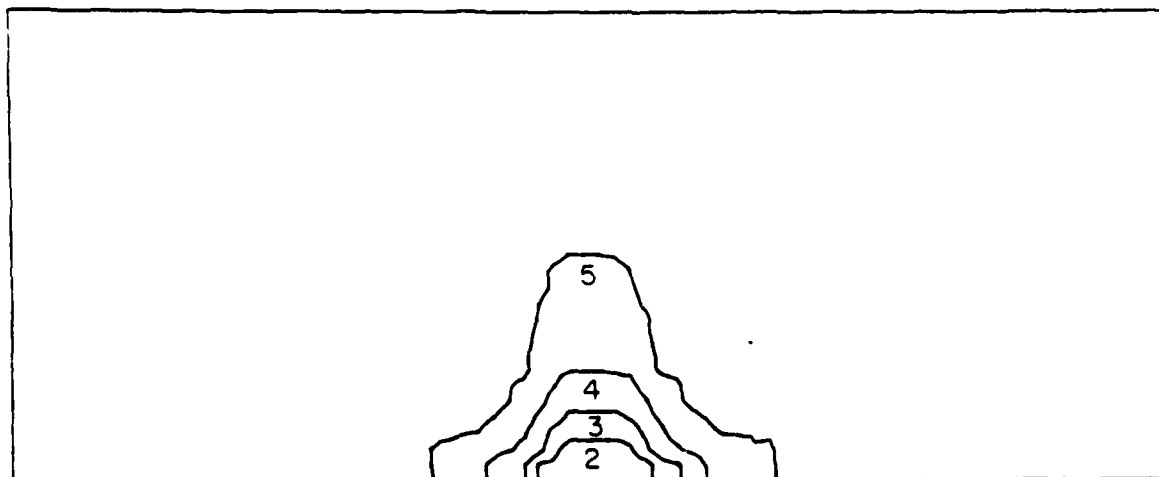


Fig. 18 — Results of a computer simulation of the time development of a laser pulse having smooth elliptical distortion. The simulation used the initial conditions described in Fig. 17. The density contour diagrams shown here correspond to the following time intervals elapsed from the point of instantaneous energy deposition: (a) $36 \mu\text{s}$, (b) $75 \mu\text{s}$, (c) 2.0 ms , (d) 4.0 ms , and (e) 6.4 ms . The six equally spaced contour values range from $7.4 \times 10^{-4} \text{ g/cm}^3$ (contour 1) to $1.26 \times 10^{-3} \text{ g/cm}^3$ (contour 6); the contour values increase with increasing vertical displacement from the center of the channel. In (a), the shock appears just inside the fine grid. Diagram (b) shows contours 1-5 and the others have only contours 2-5, indicating that the channel gas has cooled somewhat. The flattened tops of the contours result from clipping by the flux-corrected transport algorithm.

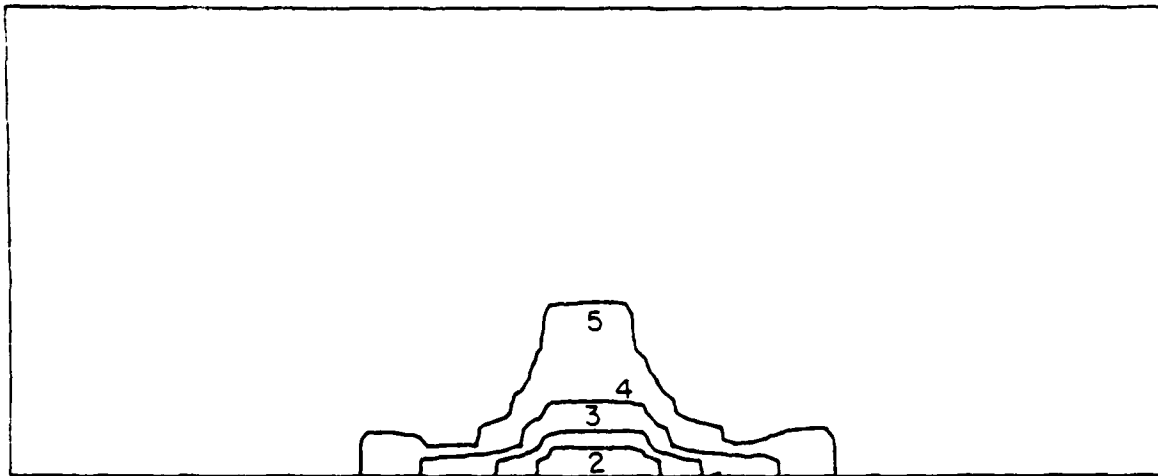


Fig. 18 — Results of a computer simulation of the time development of a laser pulse having smooth elliptical distortion. The simulation used the initial conditions described in Fig. 17. The density contour diagrams shown here correspond to the following time intervals elapsed from the point of instantaneous energy deposition: (a) 36 μ s, (b) 75 μ s, (c) 2.0 ms, (d) 4.0 ms, and (e) 6.4 ms. The six equally spaced contour values range from 7.4×10^{-4} g/cm³ (contour 1) to 1.26×10^{-3} g/cm³ (contour 6); the contour values increase with increasing vertical displacement from the center of the channel. In (a), the shock appears just inside the fine grid. Diagram (b) shows contours 1-5 and the others have only contours 2-5, indicating that the channel gas has cooled somewhat. The flattened tops of the contours result from clipping by the flux-corrected transport algorithm.

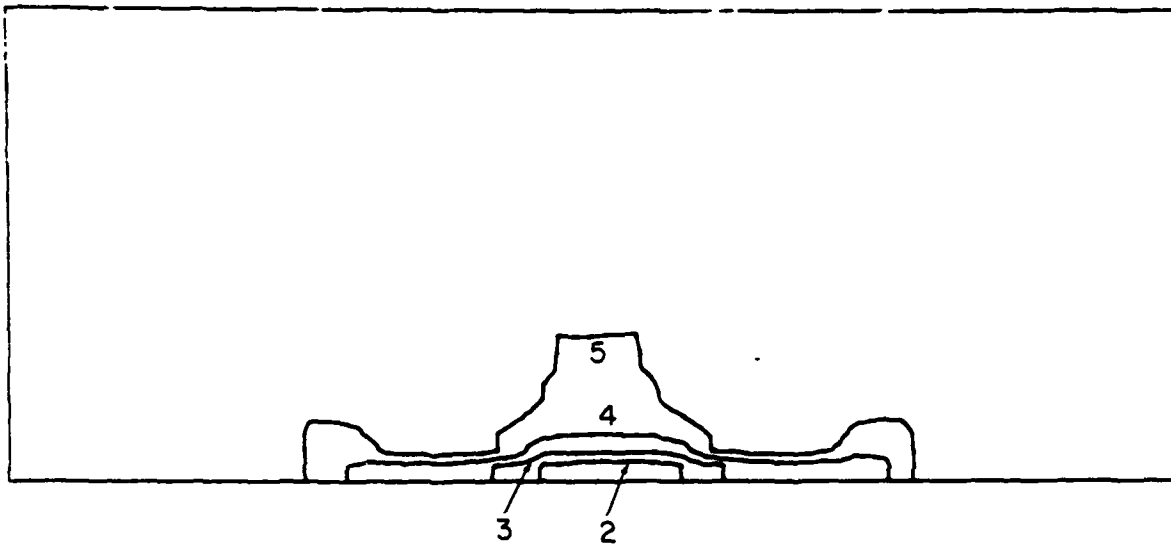


Fig. 18 — Results of a computer simulation of the time development of a laser pulse having smooth elliptical distortion. The simulation used the initial conditions described in Fig. 17. The density contour diagrams shown here correspond to the following time intervals elapsed from the point of instantaneous energy deposition: (a) 36 μ s, (b) 75 μ s, (c) 2.0 ms, (d) 4.0 ms, and (e) 6.4 ms. The six equally spaced contour values range from 7.4×10^{-4} g/cm³ (contour 1) to 1.26×10^{-3} g/cm³ (contour 6); the contour values increase with increasing vertical displacement from the center of the channel. In (a), the shock appears just inside the fine grid. Diagram (b) shows contours 1-5 and the others have only contours 2-5, indicating that the channel gas has cooled somewhat. The flattened tops of the contours result from clipping by the flux-corrected transport algorithm.

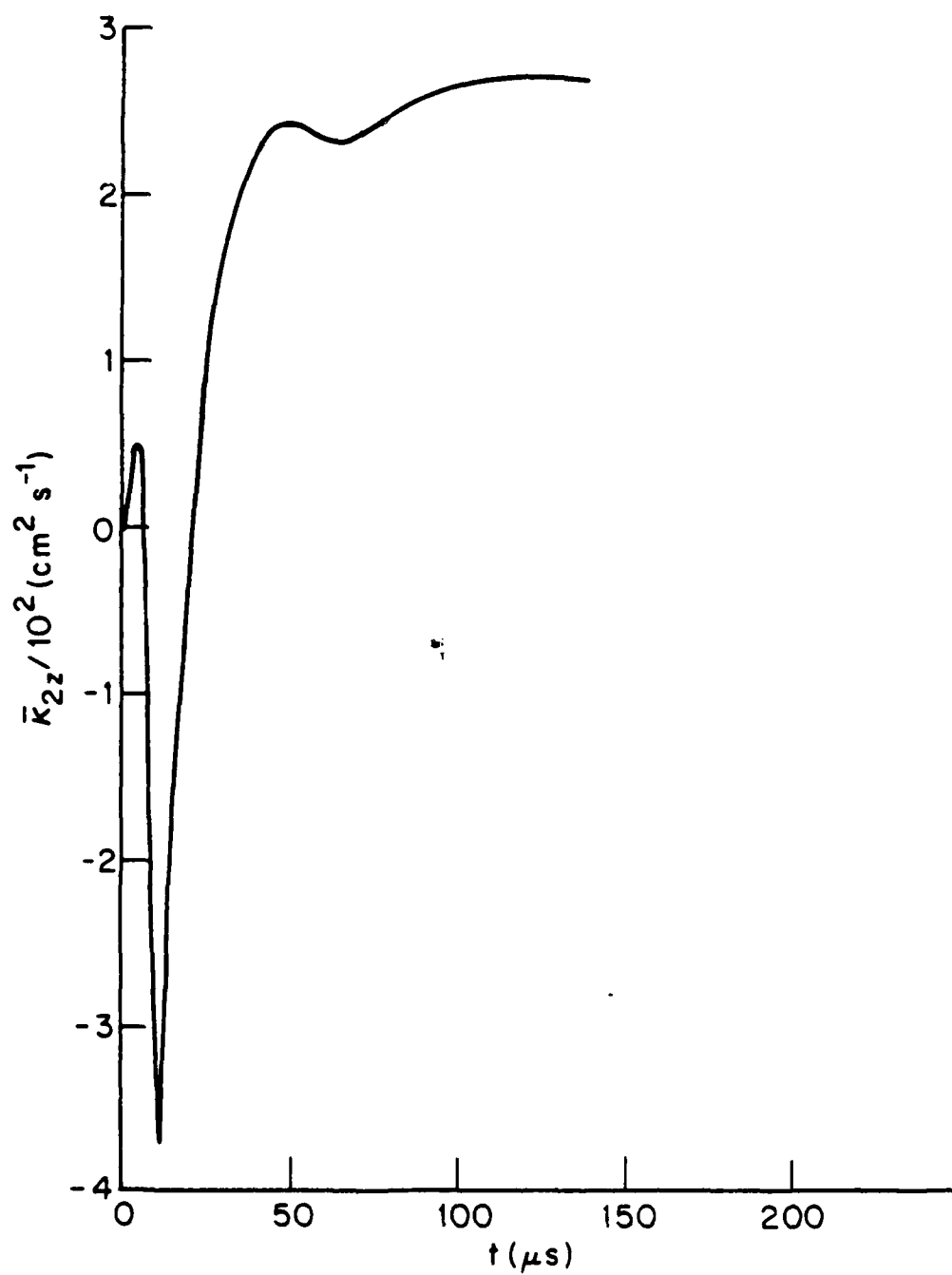


Fig 19 — The integrated vorticity $\bar{\kappa}_{2z}$ for the elliptical pulse simulation varies as shown here, with the anticipated transient behavior and a residual positive value

END

DATE
FILMED

11-82

DTIC